Wettability impact on supercritical CO_2 capillary trapping: Pore-scale visualization and quantification

Ran Hu[1,2], Jiamin Wan[2], Yongman Kim[2], and Tetsu K. Tokunaga[2]

[1] State Key Laboratory of Water Resources and Hydropower Engineering Science, Wuhan University, Wuhan, China, [2] Energy Geosciences Division, Lawrence Berkeley National Laboratory, Berkeley, California, USA

Correspondence to: J. Wan, jwan@lbl.gov

Abstract

How the wettability of pore surfaces affects supercritical (sc) CO_2 capillary trapping in geologic carbon sequestration (GCS) is not well understood, and available evidence appears inconsistent. Using a high-pressure micromodel-microscopy system with image analysis, we studied the impact of wettability on $scCO_2$ capillary trapping during short-term brine flooding (80 s, 8–667 pore volumes). Experiments on brine displacing $scCO_2$ were conducted at 8.5 MPa and 45°C in water-wet (static contact angle $\theta = 20° \pm 8°$) and intermediate-wet ($\theta = 94° \pm 13°$) homogeneous micromodels under four different flow rates (capillary number Ca ranging from 9×10^{-6} to 8×10^{-4}) with a total of eight conditions (four replicates for each). Brine invasion processes were recorded and statistical analysis was performed for over 2000 images of $scCO_2$ saturations, and $scCO_2$ cluster characteristics. The trapped $scCO_2$ saturation under intermediate-wet conditions is 15% higher than under water-wet conditions under the slowest flow rate ($Ca \sim 9 \times 10^{-6}$). Based on the visualization and $scCO_2$ cluster analysis, we show that the $scCO_2$ trapping process in our micromodels is governed by bypass trapping that is enhanced by the larger contact angle. Smaller contact angles enhance cooperative pore filling and widen brine fingers (or channels), leading to smaller volumes of $scCO_2$ being bypassed. Increased flow rates suppress this wettability effect.

1 Introduction

Immiscible fluid movement is of central importance to diverse natural and engineering processes in the subsurface, including water infiltration through soils, geological carbon sequestration (GCS) [*Pachauri et al*., 2014; *Krevor et al*., 2015], enhanced oil/gas recovery [*Patzek et al*., 2013; *Simjoo et al*., 2013], and groundwater contamination by nonaqueous liquids [*Dawson and Roberts*, 1997]. In GCS, injection of CO_2 into deep geological formations displaces native fluid (usually brine) from pore spaces, and brine later flows back to displace $scCO_2$ when the injection stops. Displacement of these immiscible fluid phases through complex pore networks results in some CO_2 becoming trapped as droplets and ganglia in pore spaces, referred to as residual trapping or capillary trapping [*Saadatpoor et al*., 2010; *Krevor et al*., 2015]. The understanding of the mechanisms underlying capillary trapping is important not only for the predictions of storage capacity in GCS

[*Saadatpoor et al*., 2010; *Krevor et al*., 2011], but also for improving the efficiency of enhanced oil/gas recovery [*Bikkina et al*., 2016].

The competition between viscous and capillary forces controls immiscible flow displacement and capillary trapping [*Lenormand et al*., 1988; *He et al*., 1992; *Wong*, 1994; *Zhang et al*., 2011b]. The fluid-fluid displacement pattern can vary from viscous fingering, capillary fingering, to stable displacement, which can be mapped into a phase diagram [*Lenormand et al*., 1988; *Zhang et al*., 2011b] using two dimensionless numbers: the capillary number Ca ($=\mu_i v_i/\sigma$, μ_i and v_i are, respectively, the viscosity and the Darcy velocity of the invading fluid, and σ is the interfacial tension) and the viscosity ratio M ($=\mu_i/\mu_d$, μ_d is the viscosity of the defending fluid). It should be noted that although a $\cos\theta$ term, where θ is the contact angle, was included in the denominator in some studies [e.g., *Jamaloei et al*., 2012; *Cao et al*., 2016], its inclusion in Ca does not fully account for influences of wettability [*Trojer et al*., 2015] because accurate scaling of capillary pressure with $\cos\theta$ is strictly limited to straight capillary tubes [*Philip*, 1971; *Anderson*, 1987]. Given that the pore structure (topology, heterogeneity, and aspect ratio) and wettability also have significant effects on the flow pattern and the resulting capillary trapping, the phase diagrams proposed by *Lenormand et al*. [1988] and *Zhang et al*. [2011b] provide a qualitative representation.

In a pioneering experimental work, *Chatzis et al*. [1983] discussed two main mechanisms for capillary oil trapping, i.e., bypass and snap-off, and investigated the effect of pore structure on the two trapping mechanisms. Their work also indicated that even though the two-pore network model (pore doublet model) [*Chatzis and Dullien*, 1983] can well describe snap-off mechanism, it fails in describing the bypass trapping when considering the fluid distribution. Later, the effects of Ca [*Chatzis et al*., 1988; *Soroush et al*., 2014; *Kimbrel et al*., 2015] and pore structure [*Tanino and Blunt*, 2012; *Chaudhary et al*., 2013; *Geistlinger et al*., 2015] on immiscible flow and capillary trapping were extensively investigated using advanced visualization technology, including X-ray computed tomography core-flooding experiments [*Krevor et al*., 2011; *Pentland et al*., 2011; *El-Maghraby and Blunt*, 2012; *Iglauer et al*., 2012; *Andrew et al*., 2013, 2014a, 2014b; *Geistlinger et al*., 2014; *Xu et al*., 2014; *Zuo and Benson*, 2014; *Li et al*., 2015; *Niu et al*., 2015; *Khishvand et al*., 2016; *Rahman et al*., 2016; *Herring et al*., 2016a, 2016b], and micromodel experiments [*Zhang et al*., 2011a, 2011b; *Wang et al*., 2012; *Kazemifar et al*., 2015, 2016; *Cao et al*., 2016; *Chang et al*., 2016a, 2016b; *Zhao et al*., 2016]. These studies indicated that (1) at Ca on the order of 10^{-7} or even smaller, the snap-off trapping mechanism by the precursor-thin film dominates, and it is enhanced by the roughness of pore surface and the throat-body aspect ratio of pores; (2) at $Ca > 10^{-7}$, the main trapping mechanism involves propagation of invading fluid fingers that lead to islands of defending fluid being bypassed.

When wettability is involved, the capillary trapping mechanism is more complicated, and conflicting results have been reported. In many studies, the trapped defending fluid saturations decreased as the medium becomes less water-wetting [*Herring et al*., 2016a], or more CO_2/oil-wetting [*Morrow*, 1990; *Iglauer et al*., 2012; *Chaudhary et al*., 2013; *Rahman et al*., 2016]. *Herring et al*. [2016a] studied the effect of wettability on residual saturation and concluded that as the contact angle increases from 5° to 42°, the residual saturation decreases. However, some studies based on measurements of drainage and imbibition capillary pressure-saturation curves in sands [*Plug and Bruining*, 2007; *Tokunaga and Wan*, 2013; *Tokunaga et al*., 2013; *Wang and Tokunaga*, 2015] suggested that trapped CO_2 saturations increase as the wettability of pore surface alters to less water-wetting. In granular porous media, greater trapping of $scCO_2$ relative to its gaseous phase has also been reported [*Plug and Bruining*, 2007; *Teng et al*., 2016], implying that the supercritical phase promotes wettability alteration of silica surfaces.

From the dynamics of fluids in porous media [*Bear,* 1972; *Dullien*, 1992], under the strong imbibition conditions (the invading fluid contact angle θ close to 0°), brine preferentially invades into smaller pores, and even advances preferentially along surface channels as corner flow [*Dong and Chatzis*, 1995; *Weislogel and Lichter*, 1998], with $scCO_2$ clusters in larger pores being bypassed [*Chatzis et al*., 1983]. The smaller contact angle will also favor the snap-off trapping within single pores. Therefore, the smaller contact angle will trap larger volume of $scCO_2$. These mechanisms of by-pass and snap-off can be well described by the pore doublet model [*Chatzis and Dullien*, 1983] and are supported by pore-network simulations [*Spiteri et al*., 2008], X-ray computed tomography (XCT) of core-flooding experiments [*Chaudhary et al*., 2013], and microfluidic experiments [*Zhao et al*., 2016].

On the other hand, other experimental results [*Cottin et al*., 2011; *Trojer et al*., 2015; *Jung et al*., 2016] and numerical simulations [*Cieplak and Robbins*, 1988, 1990] showed that as the invading fluid becomes more wetting, the fluid-fluid displacement surface becomes more stable, which enhances the displacement efficiency and results in less trapped invading fluid. The pioneering work by *Cieplak and Robbins* [1988, 1990] introduced three modes of local-scale water meniscus motion underlying the cooperative pore filling mechanism at the pore-network scale. They found that as the invading fluid becomes more wetting to the pore surface, the typical width of the invading fingers increases and appears to diverge at a critical contact angle. Later, *Holtzman and Segre* [2015] proposed a novel pore-scale model to capture the cooperative pore filling mechanism including the spatiotemporal nonlocal effects of interface dynamics. *Jung et al*. [2016] reported the crossover between stable interfacial displacement and capillary fingering in 2-D microfluidic experiments, and *Singh et al*. [2017] very recently presented the crossover in realistic 3-D porous media. These experimental and numerical works [*Cieplak and*

Robbins, 1988, 1990; *Holtzman and Segre*, 2015; *Jung et al*., 2016; *Singh et al*., 2017] support the second group of studies: increasing contact angle (invading fluid becomes less wetting) increases the $scCO_2$ trapping.

What is responsible for these two clearly different accounts for the wettability effect on the $scCO_2$ capillary trapping? Seeking to resolve the abovementioned debate on does increased contact angle increase or decrease $scCO_2$ capillary trapping, we conducted an experimental study to examine the wettability impact on the $scCO_2$ capillary trapping in both water-wet micromodels (static contact angle $\theta = 20° \pm 8°$) and intermediate-wet micromodels ($\theta = 94° \pm 15°$) in the range of capillary number *Ca* from 9×10^{-6} to 8×10^{-4} (Table 1). Based on the manufacturing process used to construct our micromodels (http://www.micronit.com/), the roughness of pore surfaces is similar to that of smooth glass beads (~0.4 μm) [*Kibbey*, 2013; *Geistlinger et al*., 2016]. Since our micromodels exhibit smooth surfaces and the capillary number is higher than the order of 10^{-7}, by-pass trapping caused by piston-like flow is predicted to govern the trapping processes [*Dullien*, 1992; *Geistlinger et al*., 2015]. Within this context, the critical question is this: does smaller contact angle (water-wet) enhance or suppress bypass trapping? As previously indicated, a smaller contact angle for invading fluid will lead to flow in smaller pores or corner flow (thin flow paths along surface channels on solids) with larger $scCO_2$ volumes being bypassed, or in contrast will induce wider flow fingers with less $scCO_2$ being bypassed. The main objective of this work is to observe and quantify how wettability impacts the bypass trapping.

Table 1. Densities, Viscosities, and Interfacial Tension of the Fluids Used in Experiment

45°C and 8.5 MPa	Brine (0.01 mol/L)	$scCO_2$
Density (kg/m^3)	993.9[a]	281.8[b]
Viscosity (kg/(s m))	5.972×10^{-4}[b]	2.2758×10^{-5}[b]
Interfacial tension (N/m)	$(33.1 \pm 0.5) \times 10^{-3}$[c]	

[a]NaCl brine density was calculated based on the regression equations of *Batzle and Wang* [1992].

[b]Density and viscosity of $scCO_2$ and the viscosity of were obtained from CO_2 phase diagram in National Institute of Standards and Technology (NIST) web-based database, available at http://webbook.nist.gov/chemistry/fluid/. Note that the viscosity of brine (0.01 mol/L) was set as the same value of water at the same temperature and pressure.

[c]Interfacial tensions for $scCO_2$-brine were measured in our laboratory using the pendant drop method [*Bachu and Bennion*, 2008].

Our micromodels are homogenous at the pore-network scale having uniform pore-throat and pore-body sizes (Figure 1b). The homogeneity of pore-network facilitates our focus on the wettability effect, rather than pore

structure heterogeneity. As reported by *Chaudhary et al*. [2013], preferential flow enhanced by water-wet angular media obscured one of the goals to investigate pore geometry controls on $scCO_2$ capillary trapping. Another advantage of our micromodels is that they can withstand up to 10 MPa pressure drop. The widely used overburden pressure cell [*Zhang et al*., 2011a, 2011b; *Wang et al*., 2012; *Chang et al*., 2016a, 2016b; *Jimenez-Martínez et al*., 2016] is not needed in our experiment system, allowing us to directly record immiscible displacement behavior at the pore scale without using dyes to enhance the difference of fluorescent signal intensity between $scCO_2$ and brine phases. Our micromodels exhibited no significant changes in contact angles before and after experiments and retained relatively uniform spatially distributed wettability (see Figure 2 and supporting information Figures S1–S5). Moreover, our visualization system permits real-time imaging of the brine invasion processes at the scale of the entire pore-network of the micromodel, thus enabling statistical analysis of capillary trapping during the entire brine flooding process. Although the wettability impact on multiphase flow has been intensively investigated [*Holtzman and Segre,* 2015; *Chaudhary et al*., 2013; *Trojer et al*., 2015; *Jung et al*., 2016; *Zhao et al*., 2016], to our knowledge, the direct visualization and quantification of the wettability impact on scCO2 capillary trapping at pore-network scale has not previously been reported.

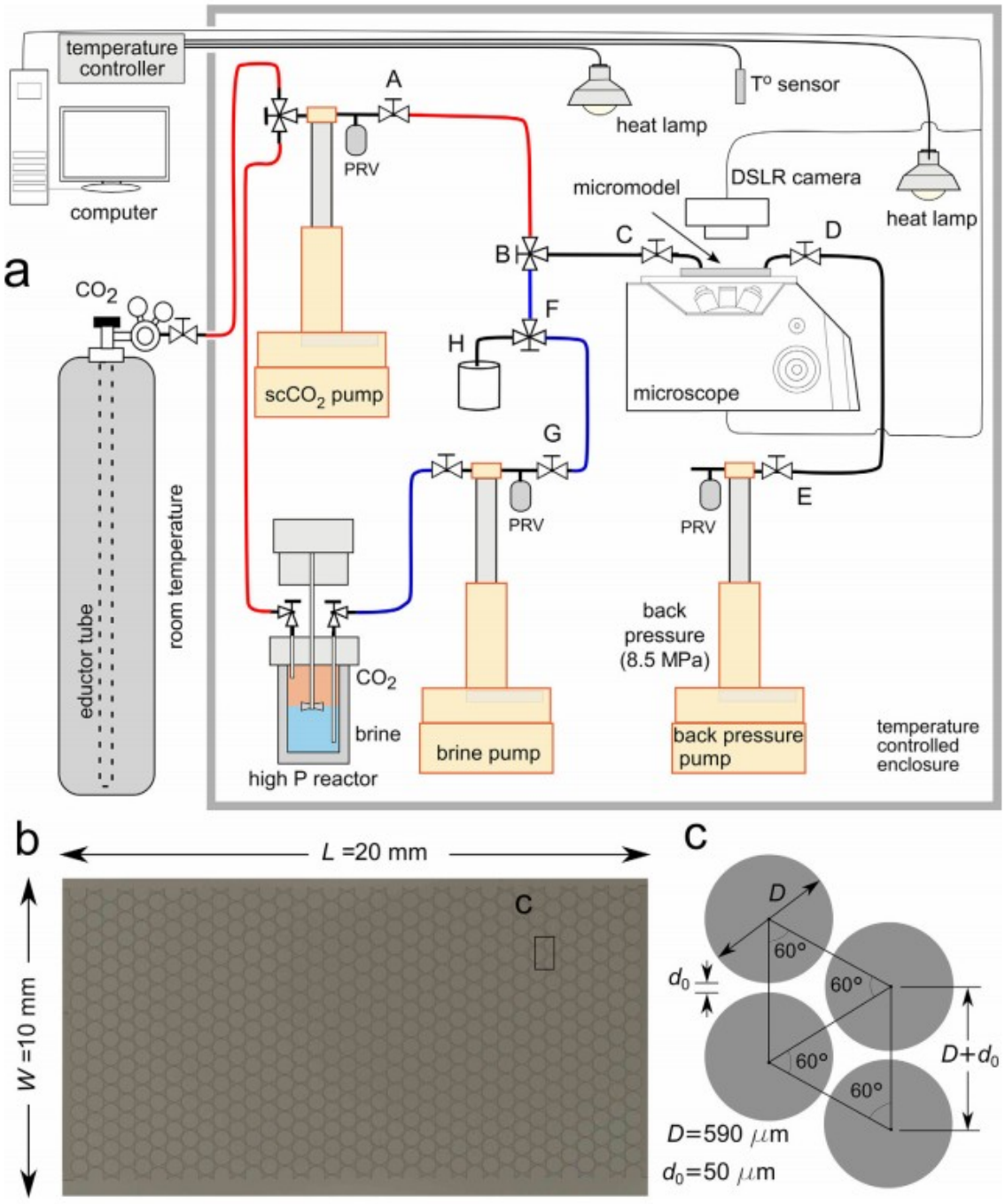

Figure 1. Micromodel experiment setup. (a) Schematic diagram, red line = $scCO_2$, blue line = brine (b) dimensions of the micromodel, composing of 576 discoid silica grains (c) the micromodel pattern, with the diameter D = 590 μm and with the depth d = 40 μm. The width of pore throat is d_0 = 50 μm.

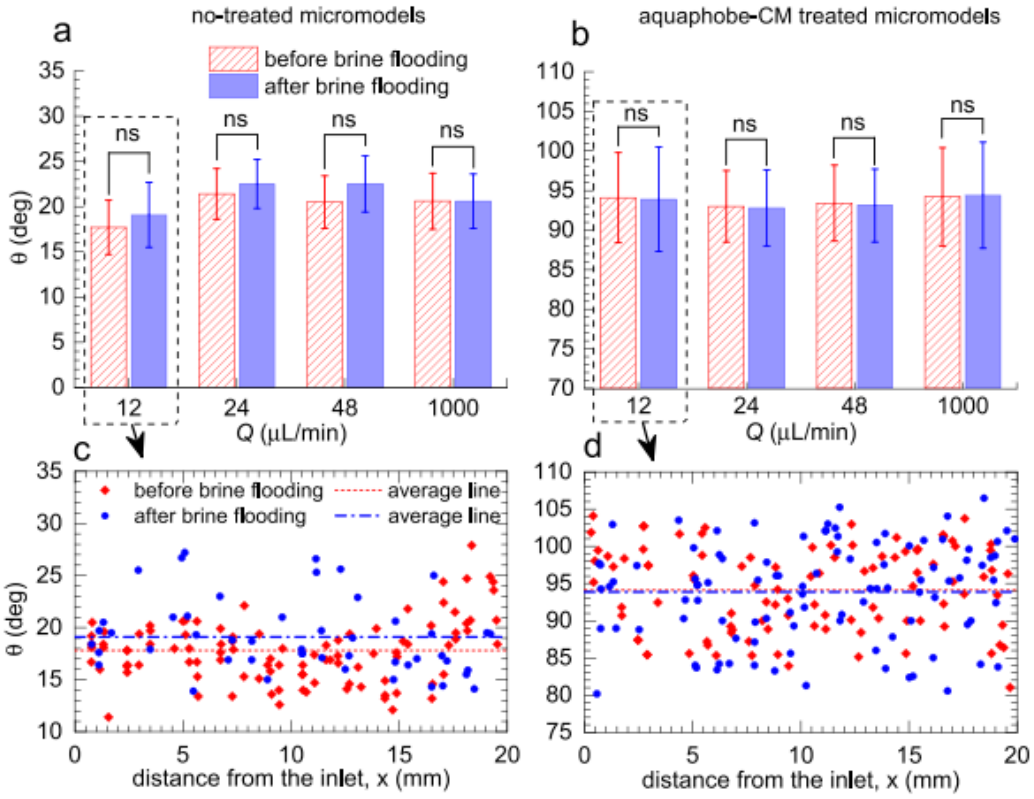

Figure 2. The contact angle measurements before and after brine flooding in (a, c) water-wet micromodels and (b, d) intermediate-wet micromodels. (a, b) The bars indicate the average values of contact angles, and the error bars indicate standard deviations. Statistically significant differences of contact angles were examined using a two-tailed Student's *t* test with unequal variance. ns indicates that average contact angle values are not significantly different ($p = 0.01$). (c, d) the variation of the measured contact angles with the distance from the inlet of the micromodels under the lowest flow rate of 12 μL/min. The average values are also shown (horizontal lines). The variation of the measured contact angles for the other three flow rate conditions can be found in supporting information Figures S1–S5.

2 Materials and Methods

2.1 High-Pressure Micromodel-Microscopy System

Figure 1a shows the high-pressure micromodel-microscopy system, which is an improvement on our previous system [*Kim et al.*, 2012]. It consists of three high-pressure syringe pumps (Teledyne ISCO, 500D/65D Syringe Pump), a CO_2 cylinder connected to an ISCO pump (labeled as $scCO_2$ pump, shown in Figure 1a), a stirred reactor (Parr, model 4560) for preparing the mutually saturated brine and CO_2 at 8.5 MPa and 45°C, a micromodel, and an imaging system. The $scCO_2$ pump is used to fill the brine-saturated $scCO_2$ into the micromodel during $scCO_2$ flooding, whereas the brine pump (see the label in Figure 1a) injects the CO_2-saturated brine to displace previously stored $scCO_2$ in micromodel during brine flooding. The back-pressure pump keeps the flow system at a constant pressure of 8.5 MPa.

The imaging system has an inverted microscope (Carl Zeiss, Observer Z1.m) operated in two modes: one utilizes a CCD camera (Carl Zeiss, AxioCam MRc5) that records images at the pore scale, and another utilizes a DSLR camera (Nikon, D90) installed over the stage of the inverted microscope to

record images of the full pore network of the micromodel. The inverted microscope includes two reflecting light objectives. One is the objective Epiplan 5×/0.13 W0.8″ (working distance =20.5 mm) which captures the fluid distribution within four to five pores with a spatial resolution of 2.0 μm/pixel, and the other is the objective EC Epiplan 20×/0.4 M27 (working distance =3.2 mm) which records the flow behavior within single pore with a spatial resolution of 0.5 μm/pixel. The DSLR camera (Nikon, D90) has APS-C size sensor 23.6 mm × 15.8 mm, 12.30 Megapixels, which provides a spatial resolution of 4.1 μm/pixel for the entire domain of the micromodels. The entire experimental system is contained in an insulated enclosure to maintain the temperature at 45 ± 1°C during the experiments (Figure 1a).

2.2 Micromodels and Wettability Alteration

The micromodels used in this study were fabricated by Micronit Microfluidics BV (Figure 1b). After the designed homogeneous pore network was etched on the silica plates with hydrofluoric acid, two symmetrically patterned plates were fused together. Direct aligned bonding of the two plates was performed by creating a so-called prebond between two wafers, which was then annealed at high temperature. Given the strong bonding, the micromodels can be operated under the pressure difference (inside relative to outside) up to 10 MPa. The pore volumes (PV) is 1.97 μL and the porosity is 0.245. To alter the wettability of a micromodel, a coating solution was prepared by diluting Aquaphobe-CM (PP1-AQCM, Gelest) with hexane (ACS grade, EMD). A 5% (v/v) Aquaphobe-CM solution was used [*Hu et al*., 2017]. The coating solution was injected into a micromodel at 1 mL/h for 2 h in order to saturate the micromodel with the coating solution. Then, the inlets and outlets of the micromodel were kept closed for overnight at ambient pressure and temperature to allow enough time for the coating solution to react with the surface of micromodel. Then, the hexane was injected to clean the micromodel at the flow rate of 0.2 mL/min for 10 min (3 times). Next, 8 mL of air was injected into the micromodel at 0.8 mL/min for 10 min, 3 times in order to remove the hexane from the micromodel. After that, the micromodel was dried and cured at 100°C for 1 h. The average contact angle of the Aquaphobe-CM-treated micromodels is listed in Table 3.

2.3 Preparing the $scCO_2$-Saturated Brine and the Brine-Saturated $scCO_2$

Inside the thermal insulation chamber, the clean CO_2 from a cylinder (99.99% purity, Airgas) was pressurized within the $scCO_2$ ISCO pump (Figure 1a) to its supercritical state under 45°C and 8.5 MPa. The pressure represents reservoir conditions at depths near 1.0 km [*Metz*, 2005]. The brine (0.01 M NaCl) was prepared using deionized (DI) water (EMD Millipore, Milli-Q) and NaCl (Sigma-Aldrich, ACS grade). To prepare the mutually saturated brine and CO_2, the degassed brine was injected into the Parr reactor (Figure 1a), and then CO_2 was transferred to the reactor and pressurized. After 24 h of stirring under 8.5 MPa and 45 ± 1°C, the brine and

$scCO_2$ were ready for use. The fluid properties were obtained from the literature under similar conditions, as listed in Table 1.

2.4 Experimental Procedures

A clean micromodel was assembled and fixed on the microscope stage. The degassed brine was first injected into the micromodel with the back-pressure pump at a slow flow rate (12 μL/min, 10 s/PV) at atmosphere pressure to completely displace the air (flow path: E → D → C → B → F → H). After the micromodel was fully saturated with brine, the three-way valve F was closed and the back-pressure pump was used to increase pressure to 8.5 MPa. After that, the three-way valve F was switched on to the brine pump. The brine pump injected the $scCO_2$-saturated brine into the micromodel to displace the initial brine (non-$scCO_2$-saturated) at a flow rate of 480 μL/min for 20 min via flow path of G → F → B → C → D → E. After 20 min, the micromodel could be completely saturated with CO_2-saturated brine. Then the three-way valve B switched on to the $scCO_2$ pump and the $scCO_2$ injection port A was opened. Transient brine phase movement resulting from valve switching was allowed to settle down by statically equilibrating the system (45°C, 8.5 MPa) for 30 min. Given the focus of this study on trapping following brine flooding, it was important to establish very similar initial $scCO_2$ saturations for all brine flooding experiments. Therefore, after 30 min the $scCO_2$ was injected into the micromodel by the $scCO_2$ pump at a constant flow rate (1000 μL/min) to displace brine for 60 s (500 PV) and obtain similar initial $scCO_2$ saturations for both the untreated and treated micromodels (Table 2). The three-line valve B then was switched to the brine pump to allow the system to hydrostatically equilibrate (45°C, 8.5 MPa) for 30 min. Pore-scale images were taken after the equilibrium stage for initial contact angle measurements.

Table 2. Summary of Experiment Conditions

Exp. #	Wettability	Q (μL/min)	Ca	Brine Injected per Second (PV)	Total Injected Brine (PV)	Initial $scCO_2$ Saturation, S_i (%)
1–4	Water-wet	12	9.0×10^{-6}	0.1	8	61.6 ± 0.7
5–8		240	1.8×10^{-4}	2	160	64.6 ± 3.9
9–12		480	3.6×10^{-4}	4	320	61.1 ± 1.2
13–16		1000	7.5×10^{-4}	8.5	667	63.4 ± 0.6
17–20	Intermediate-wet	12	9.0×10^{-6}	0.1	8	62.8 ± 1.1
21–24		240	1.8×10^{-4}	2	160	62.6 ± 2.0
25–28		480	3.6×10^{-4}	4	320	64.0 ± 3.4
29–32		1000	7.5×10^{-4}	8.5	667	65.5 ± 0.9

After 30 min, brine flooding initiated with constant flow rates of 12, 240, 480, and 1000 μL/min for 80 s. During this step, images of $scCO_2$ phase in the entire micromodel were recorded at 1 frame/s with the DSLR camera (Nikon, D90). The selection of relatively short 80 s runs was based on achieving quasi-steady conditions well within that time frame, and the need for replicate runs under many flow conditions. Here the quasi-steady conditions indicate that the average changes of $scCO_2$ saturation became less than

0.1% per second. After 80 s of brine flooding, the imaging system was switched to the inverted microscope, and higher-resolution images of $scCO_2$ phase distributions in single pore using the objective EC Epiplan 20×/0.4 M27 (WD = 3.2 mm) and in multiple pores using the objective Epiplan 5×/0.13 W0.8″ (WD = 20.5 mm) were recorded, which facilitated the determination of contact angles. For our imaging system, although the video mode of the DSLR camera enables us to take movies of brine flooding processes, the image resolution in this video mode is too low to perform quantitative calculations of saturations. Therefore, invasion morphology was only imaged at a frequency of one frame per second, the maximum capture rate for high-resolution photographs obtainable with the DSLR camera. After the experiment, the micromodel was depressurized to the room pressure and then cleaned by injecting DI water at the flow rate of 12 μL/min for 5 min.

The above procedures were applied to both water-wet and intermediate-wet micromodels and each wetting and flow rate condition was repeated four times for a total of 32 experiments. The sequence of experiments is given in Table 2, showing that at the flow rates of 12, 240, 480, and 1000 μL/min, and one PV of brine is injected within only 10, 0.5, 0.25, and 0.012 s, respectively.

The relative effect of viscous forces to the capillary forces can be quantified by the classic macroscopic capillary number *Ca* [*Lenormand et al*., 1988; *Zhang et al*., 2011b; *Chaudhary et al*., 2013; *Geistlinger*, 2015]. As noted in *Blunt and Scher* [1995], the classic macroscopic capillary number cannot consider the scales that the two forces act on, because the viscous force acts on the nonlocal scale and is a kind of volumetric force and the capillary force acts on the interface of the water menisci [*Armstrong et al*., 2014]. In this study, however, to compare the order of magnitude of *Ca* with the literature [*Lenormand et al*., 1988; *Zhang et al*., 2011b; *Chaudhary et al*., 2013; *Geistlinger*, 2015], the classic macroscopic capillary number *Ca* was adopted by $Ca = v_i \mu_{brine}/\sigma$, where v_i is the mean Darcy velocity, $v_i = Q/A_c$, Q is the volume flow rate, A_c is the cross-section area of the near-inlet, $A_c = W \times d = 10$ mm × 40 μm (Figure 1). With this convention, *Ca* ranges from 7.5×10^{-4} to 9.0×10^{-6}, spanning 2 orders of magnitude (Table 2).

2.5 Contact Angles Before and After Experiments

Since the wettability is the main focus of this work, it is critical to evaluate the variation of contact angles before and after experiments. For the no-treated micromodels, *Kim et al*. [2012] reported that due to the reaction with $scCO_2$ and brine, the contact angle of silica surface can significantly increase during drainage and a longer-term exposure to $scCO_2$ flow. For the Aquaphobe-CM-treated micromodels, the coating treatment may be unstable and the wettability of treated micromodels may change back to water-wetting. Moreover, the silanization of the micromodel can also lead to heterogeneous wettability [*Karadimitriou*, 2013]. Using ImageJ software

[*Abràmoff*, 2004] combined with a contact angle plug-in (Marco Brugnara, marco.brugnara@ing.unitn.it), we measured contact angles before and after the experiments for each flow rate conditions and for untreated and treated micromodels. To isolate the effects caused by the location of measurements, the image of the micromodel (20 mm × 10 mm, 4.1 μm/pixel) captured by the DSLR camera was divided into 50 subzones of 2 mm × 2 mm, and in each subzone two menisci were selected to measure the contact angles. We also measured the contact angles based on the images captured by the microcopy. The details of contact angle measurements can be found in the supporting information Figures S1–S5.

Figure 2 shows the comparisons of the measured contact angle before and after brine flooding. Based on a two-tailed Student's t test ($p = 0.01$) (Figures 2a and 2b), no significant wettability changes were observed before and after brine flooding both in the no-treated micromodels (Figure 2a) and in treated micromodels (Figure 2b) for each flow rate conditions. Figures 2c and 2d further demonstrate that the values of contact angles at different locations are random. Thus, there is no patterned wettability zonation in our treated/nontreated micromodels, and hence the effect of wettability heterogeneity can be neglected in this study. Table 3 summarizes the measured values of the contact angles, showing that in the nontreated micromodels, contact angle ranges from 11.4 to 27.9°, and it ranges from 79.4 to 106.5° in the treated micromodels. The changes of average values ($\Delta\theta_{avg}$) and median values ($\Delta\theta_{med}$) of contact angles for different flow rate conditions are $\Delta\theta_{avg} \leq 4.8°$ and $\Delta\theta_{med} \leq 5.1°$ in the nontreated micromodels and $\Delta\theta_{avg} \leq 2.9°$, $\Delta\theta_{med} \leq 5.2°$ in the treated micromodels. From the above consideration, we can conclude that our silica surfaces (untreated and treated) were stable under the experimental conditions (8.5 MPa and 45°C) with uniform wettability.

Table 3. Summary of the Measured Contact Angles Before and After Brine Flooding

		Before Brine Flooding			After Brine Flooding		
	Q (μL/min)	$\theta_{min} \leq \theta \leq \theta_{max}$ (°)	θ_{med}[a] (°)	θ_{avg}[b] $\pm$ θ_{SD}[c] (°)	$\theta_{min} \leq \theta \leq \theta_{max}$ (°)	θ_{med} (°)	$\theta_{avg} \pm \theta_{SD}$ (°)
Untreated	12	$11.4 \leq \theta \leq 27.9$	17.8	17.7 ± 3.0	$13.9 \leq \theta \leq 27.2$	18.4	19.1 ± 3.6
	240	$16.1 \leq \theta \leq 27.5$	21.0	21.4 ± 2.8	$18.1 \leq \theta \leq 27.7$	22.6	22.5 ± 2.7
	480	$15.2 \leq \theta \leq 27.4$	20.7	20.5 ± 2.9	$17.4 \leq \theta \leq 27.2$	22.9	22.5 ± 3.1
	1000	$14.0 \leq \theta \leq 26.6$	20.6	20.6 ± 3.1	$16.0 \leq \theta \leq 26.2$	20.2	20.6 ± 3.0
	All[d]			$\theta_{avg} = 20.2$, $11.4 \leq \theta \leq 27.9$			
Treated	12	$81.0 \leq \theta \leq 104.1$	95.2	94.1 ± 5.7	$80.2 \leq \theta \leq 106.5$	94.8	93.9 ± 6.6
	240	$85.2 \leq \theta \leq 103.4$	93.0	93.0 ± 4.5	$85.4 \leq \theta \leq 104.0$	91.1	92.8 ± 4.8
	480	$85.3 \leq \theta \leq 104.5$	93.1	93.4 ± 4.8	$85.3 \leq \theta \leq 104.0$	93.0	93.1 ± 4.6
	1000	$79.4 \leq \theta \leq 105.3$	95.7	94.2 ± 6.2	$80.3 \leq \theta \leq 105.2$	96.3	94.4 ± 6.7
	All[d]			$\theta_{avg} = 93.6$, $79.4 \leq \theta \leq 106.5$			

[a,b,c] θ_{med}, θ_{avg}, and θ_{SD} are the median, average, and standard deviation of the contact angles, respectively; the range and the average/standard deviation of the contact angles are calculated from the measurements from images captured by DSLR camera (supporting information Figures S1–S4) and captured by microscopy (supporting information Figure S5). The aggregated average values and ranges of θ are provided in the row "all" for untreated and treated micromodels.

2.6 Image Analysis

To avoid their potential influence on the pore surface wettability, a fluorescent dye was not employed and hence there is no large difference in signal intensity of the images captured by DSLR camera between the brine and $scCO_2$ phases. Moreover, the raw images from DSLR camera show that the light intensity in the left zone ($x \leq 10$ mm, x is the distance from the inlet) is slightly higher than that in right zone ($x > 10$ mm) (supporting information Movies S1–S8), which would modify the contrast between $scCO_2$ and brine and hence the threshold value. The nonuniform light intensity suggests that the micromodel plane in length and width (20 mm × 10 mm) is not absolutely parallel to plane of the sensor (23.6 mm × 15.8 mm) of DSLR camera. Any small perturbation of the distance between the two planes would cause nonuniform distribution of the light intensity in the images. To isolate the contrast-affected regions and to identify individual clusters and ganglias of $scCO_2$ in the raw images, the following procedures were applied based on MATLAB Image Processing Toolbox. The raw images were first divided into two parts (supporting information Figure S7), and then the morphological opening method with a disk-shaped structuring element was performed by recalling the function of *imopen* in MATLAB to estimate the background illumination for each part. The background illumination was then subtracted from two sub-images, followed by increasing the images contrast separately. Two binary images were created by thresholding the subimages using Otsu's method [*Otsu*, 1975] which chooses the threshold value to minimize the intraclass variance of the thresholded black (brine) and white ($scCO_2$) pixels. After the combination of the two binary images, the $scCO_2$ saturation and each $scCO_2$ clusters can be identified. The details of these steps are illustrated in supporting information Figures S6–S7. To evaluate this method, we compared the calculated porosity from the image of fully saturated with air with the designed porosity. A good agreement with the relative error <2% was obtained. We also performed statistical analysis of the $scCO_2$ clusters during all the brine flooding processes (80 images × 32 experiments). For each image, the equivalent radius (r_i) of single $scCO_2$ clusters, as the radius of a circle of the same area: $r_i = \sqrt{A_i/\pi}$, where A_i is the cluster area. The average cluster radius (r_{avg}), the maximum cluster radius (r_{max}), and the standard deviation of cluster radius (r_σ) were calculated, respectively, by

$$r_{avg} = \frac{1}{N}\sum_{i=1}^{N} r_i, \quad (1)$$

$$r_\sigma = \sqrt{\frac{1}{N}\sum_{i=1}^{N}\left(r_i - r_{avg}\right)^2}, \quad (2)$$

$$r_{max} = \max\left\{r_1, r_2, \ldots, r_N\right\}, \quad (3)$$

where N is the total number of clusters.

3 Results and Discussion

3.1 $scCO_2$ Flooding

In GCS after the long-term CO_2 injection phase (can last for decades) the CO_2 saturation can approach its maximum in many locations. At the beginning of brine flooding (500 PV of $scCO_2$ injected during the $scCO_2$ flooding processes), the average $scCO_2$ saturations are in the range of 61.1–65.5% (Table 2), and representative $scCO_2$ cluster distributions are presented in supporting information Figure S8. The very high flow rate used to establish initial conditions helped to minimize the differences between the $scCO_2$ saturation at the end of $scCO_2$ flooding processes in the water-wet and intermediate-wet micromodels.

3.2 Brine Flooding and $scCO_2$ Capillary Trapping

During the brine flooding processes, the brine phase was injected at the constant flow rates of 12, 240, 480, and 1000 μL/min (Table 2). The final residual $scCO_2$ saturation was defined as its value at 80 s of brine flooding, where the average changes became less than 0.1% per second. We observed that the $scCO_2$ saturations became relatively stabilized after about 5–10 s for all the experiment conditions. This study focused on understanding the early stage trapping, recognizing that over the much longer times associated with GCS, $scCO_2$ dissolution, redistribution of trapped phases, and mineral trapping [*Xu et al*., 2005] are all important. These much longer time scale processes are beyond the scope of these short-term experiments.

We selected the binary images at 80 s as representative of the brine invasion morphology. The movies showing the entire brine flooding processes can be found in the supporting information Movies S1–S8. Figure 3 shows the typical trapped $scCO_2$ saturation at 80 s. The images clearly present that $scCO_2$ saturation in water-wet micromodel is lower than that in the intermediate-wet micromodel at all the flow rates. Examples of $scCO_2$ clusters within single and multiple pores recorded by microscopy are shown in Figure 4. The curvatures of $scCO_2$-brine interfaces in the water-wet case are clearly larger than that in intermediate-wet micromodel. The $scCO_2$ clusters occupy a single pore body or span several pore bodies connected by pore throats [*Geistlinger et al*., 2015]. As observed in Figure 4b ′, the brine appears as droplets due to water accumulating in the less water-wet pore surface [*Kim et al*., 2012].

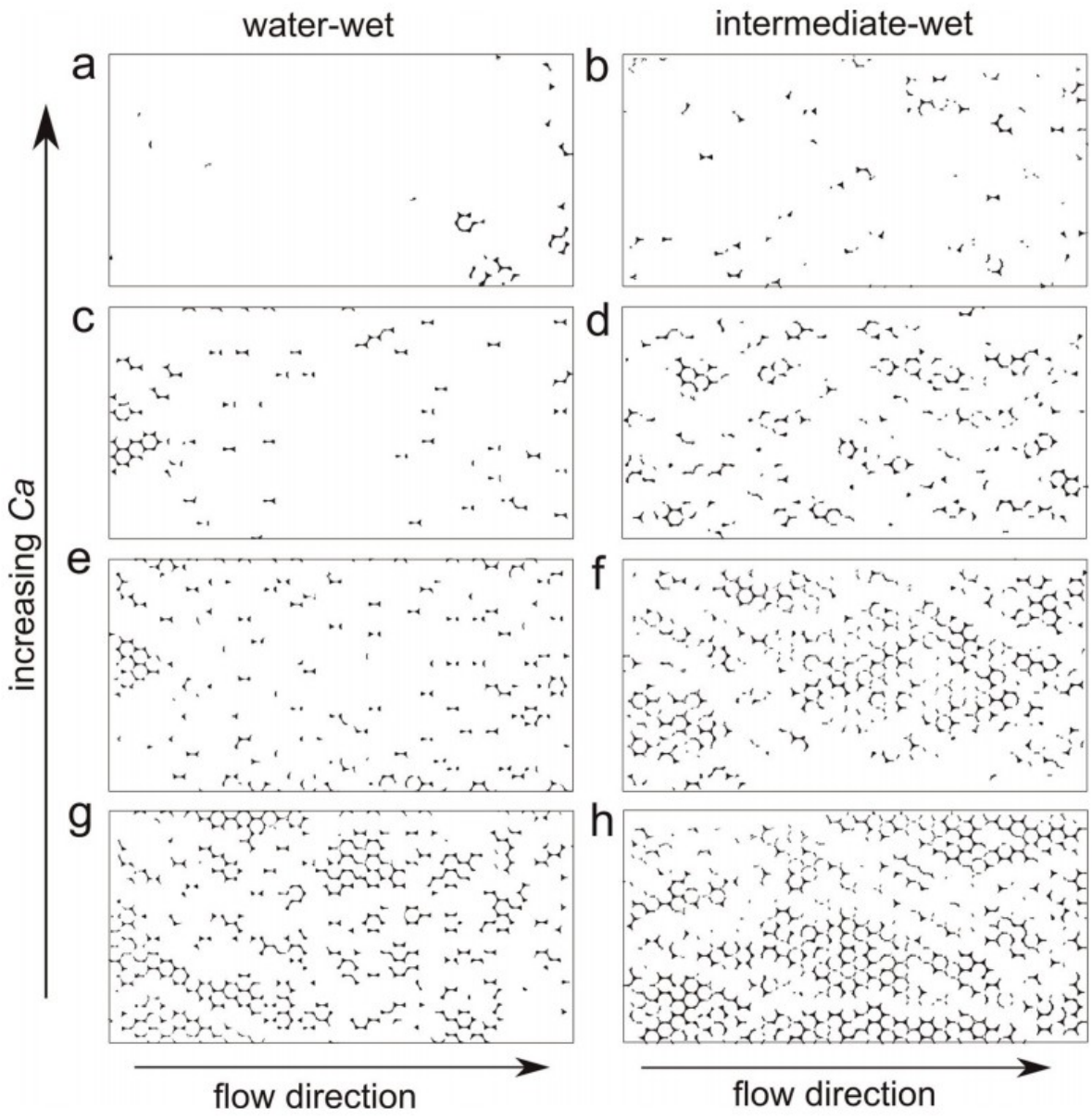

Figure 3. Representative $scCO_2$ saturation and cluster distributions at 80 s of brine flooding at flow rates of (a, b) $Ca = 9.0 \times 10^{-6}$, $Q = 1000$ μL/min, (c, d) $Ca = 1.8 \times 10^{-4}$, $Q = 480$ μL/min, (e, f) $Ca = 3.6 \times 10^{-4}$, $Q = 240$ μL/min, and (g, h) $Ca = 7.5 \times 10^{-4}$, $Q = 12$ μL/min. The left and right columns show images of the water-wet and intermediate-wet micromodels, respectively. The dark color is residual $scCO_2$, and the brine and solid phase are not shown. By 80 s, the change of average $scCO_2$ saturation for all four replicates is less than 0.1%/s, and the remaining $scCO_2$ is referred as capillary trapped $scCO_2$. The measured $scCO_2$ saturations from top down for the water-wet case are (a) 2.5%, (c) 7.2%, (e) 14.8%, and (g) 27.6%, and for the intermediate-wet case are (b) 4.6%, (d) 14.7%, (f) 27.2%, and (h) 41.5%. The trapped $scCO_2$ saturations for the other 24 experiments are listed in supporting information Table S1.

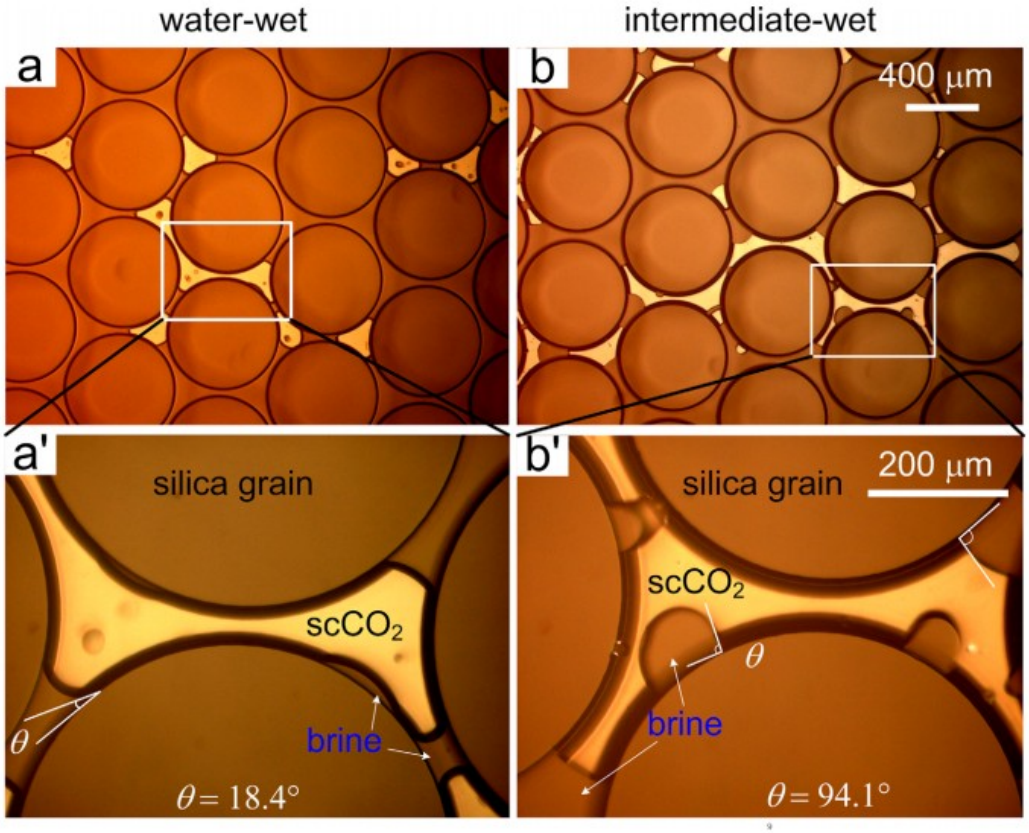

Figure 4. Typical shapes/structures of trapped $scCO_2$ clusters within single pores and multiple pores of the (a, a′) water-wet and (b, b′) intermediate-wet experiments at flow rate 12 μL/min. The lighter color is $scCO_2$ and the darker is brine. The measured contact angles shown in (a′) is 18.4° for the water-wet and 94.1° for the intermediate-wet micromodels.

Based on the analyses of over 2500 images, we obtained the relationships between $scCO_2$ saturation (S_{CO2}) and injected brine PVs and brine flooding time (Figure 5). We chose to report the S_{CO_2} values at 80 s as the residual saturation $S_{CO_2,r}$, by which time the ΔS_{CO_2} became <0.1% per second. The S_{CO_2} experienced rapid changes at the beginning a few seconds (the gray colored region is the first 5 s). Then the S_{CO_2} quickly (between 6 and 10 s) reached to near the steady state. Continued brine flooding resulted in only small changes. The rates of decline in S_{CO_2} within the first 5 s, do not exhibit a consistent trend with respect to variations in Q. At $Q = 12$, 240, and 1000 μL/min, S_{CO_2} declines with a higher rate in water-wet case, whereas at $Q = 480$ μL/min, no remarkable differences in the rate of S_{CO_2} decline were observed. At the lowest flow rate of 12 μL/min ($Ca = 9.0 \times 10^{-6}$), brine flooding resulted in 90% of final $scCO_2$ residual trapping within the initial 0.5 PV (Figure 5a), similar to results reported for core-flooding experiments on carbonate rocks under spontaneous imbibition conditions [*Niu et al.*, 2015; *Al-Menhali and Krevor*, 2016]. However, for the higher flow rates ($Ca = 1.8 \times 10^{-4}$, 3.6×10^{-4}, and 7.5×10^{-4}), a continuous decrease in the $scCO_2$ saturation after 5 s was observed. This is because the $scCO_2$ clusters were mobilized and removed from the micromodel as a result of the higher viscous pressure drop

under higher flow rate conditions, which were reflected by the cluster number evolution in the Figures 6a and 6b.

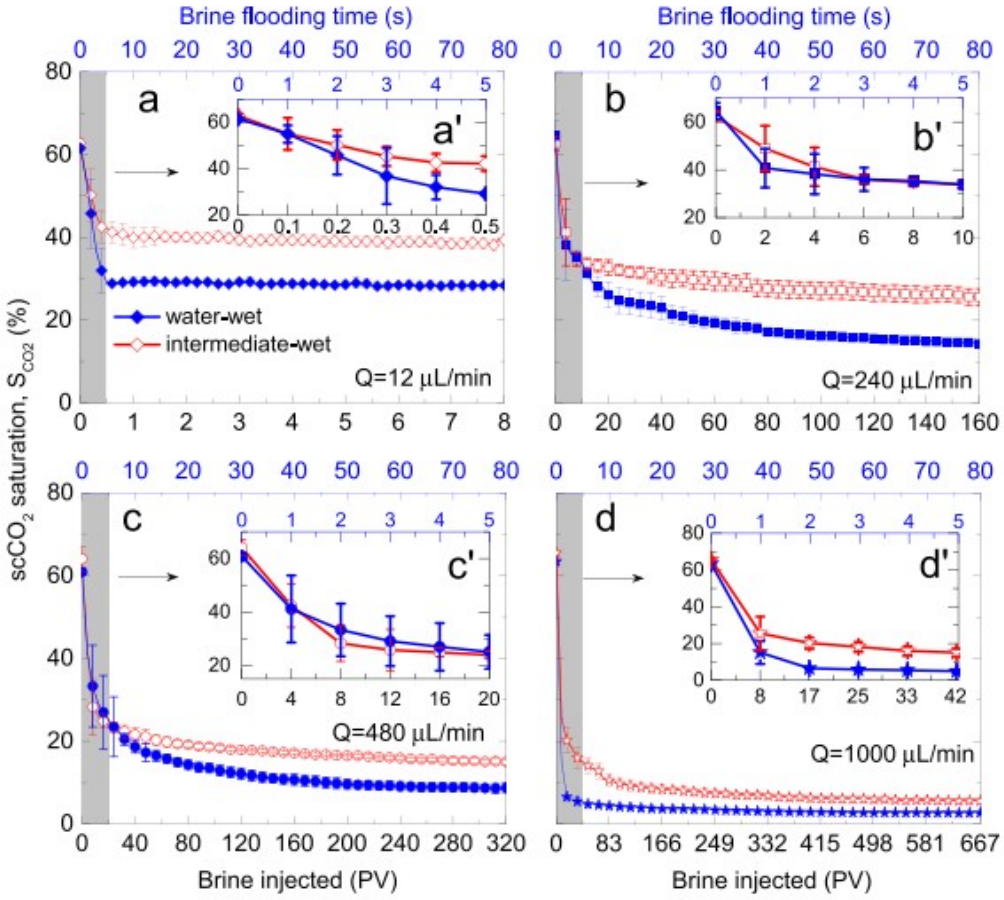

Figure 5. The decline in $scCO_2$ saturation with injected brine pore volumes and with brine flooding time at flow rates of (a) $Q = 12$ μL/min, (b) $Q = 240$ μL/min, (c) $Q = 480$ μL/min, and (d) $Q = 1000$ μL/min. The solid (◆, ■, ●, ★) and open (◇, □, ○, ⋆) symbols indicate, respectively, the water-wet and intermediate-wet cases. The evolutions of $scCO_2$ saturation within the first 5 s of brine flooding time are shown in (a′), (b′), (c′), and (d′), corresponding to injections of 1, 20, 40, and 83 PV of brine, respectively. The data points indicate the average saturation of four replicate experiments, and the error bars indicate standard deviations.

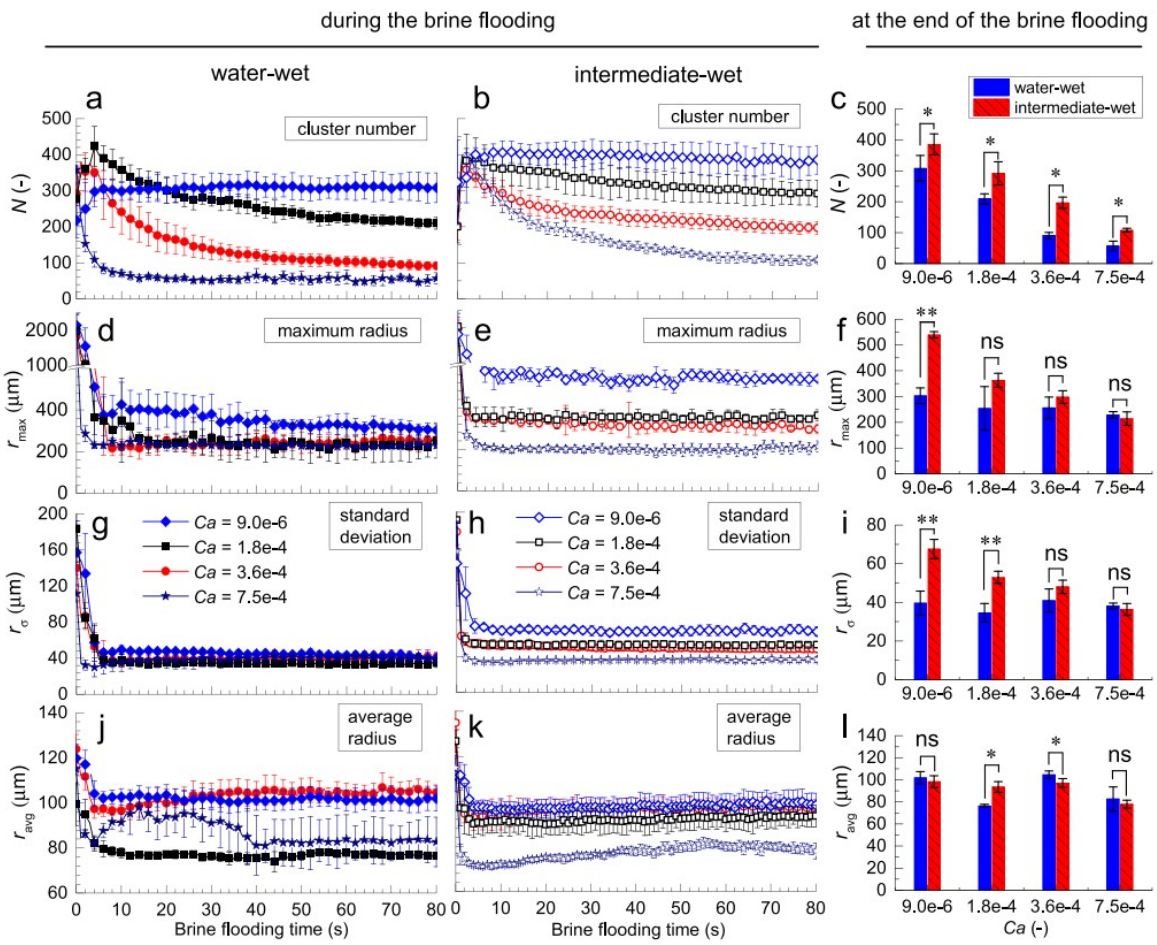

Figure 6. The $scCO_2$ cluster characteristics during the brine flooding processes in water-wet (a, d, g, j) and intermediate-wet micromodels (b, e, h, k). (a, b) Total cluster number, *N*, (c, d) maximum cluster radius, r_{max}, (e, f) standard deviation of the cluster radii, r_σ, (g, h) average cluster radius, r_{avg}. Statistically significant differences of (c) *N*, (f) r_{max}, (i) r_σ, and (l) r_{avg} at the end of the brine flooding were examined using a two-tailed Student's *t* test with unequal variance; $^*p \leq 0.05$, $^{**}p \leq 0.01$, ns denotes no significant difference ($p > 0.05$) between water-wet and intermediate-wet cases. Each data point is the average of four replicate experiments, and the error bars indicate standard deviations.

The results show higher S_{CO_2} under the intermediate-wet condition than that under the water-wet condition, and the trend is consistent for all the flow rates. At the lowest flow rate ($Q = 12$ μL/min, $Ca = 9.0 \times 10^{-6}$), the difference of the $S_{CO_2,f}$ is ~15% ($S_{CO_2,f} = 27$ and 43% for the water-wet and intermediate-wet, respectively). We believe that the difference would become even larger if the flow rate was further decreased, closer to typical reservoir flow rates ($Ca < 10^{-7}$). Unfortunately, such low flow rates could not be achieved with good control because of limitations of the lowest pump flow rate together with the very small PV (2 μL) of the micromodel. Nevertheless, the data unambiguously indicate the $S_{CO_2,f}$ is higher in the less water-wet media. This wettability effect became less significant when the flow rate increased. If the flow rate were further increased to the degree that the capillary force no longer applies the role and the viscose force became overwhelmed, the wettability effect should vanish.

3.3 Statistical Analysis of $scCO_2$ Clusters

To understand how the $scCO_2$ phase is distributed within the porous medium during the brine flooding, we performed statistical analysis of $scCO_2$ clusters. Figure 6 shows that the average radius (r_{avg}), the maximum radius (r_{max}), and the standard deviation (r_σ) of clusters declined dramatically at the initial times of brine flooding, whereas the total number of $scCO_2$ clusters N (except the condition of water-wet case with 1000 μL/min, Figure 6a) increased considerably at the beginning of brine flooding (Figures 6a and 6b). The reason is that larger $scCO_2$ clusters broke up and smaller clusters were generated, and thus the cluster distributions tended to be more uniform (decreasing r_σ). In the water-wet case with the highest flow (1000 μL/min), $scCO_2$ displaced from the micromodel is dominant over breakup events of $scCO_2$ clusters, and lead to a decrease in $scCO_2$ cluster number. The breakup events have been observed in carbonate rock in core-flooding experiment [*Pak et al*., 2015], in unconsolidated packs of glass spheres [*Wardlaw and McKellar*, 1985] and have been reproduced by stochastic simulation [*Ng and Payatakes*, 1980].

After 5 s of brine flooding, for the slowest flow rate (closer to reservoir conditions, $Ca = 9.0 \times 10^{-6}$), the total cluster number N kept constant (Figures 6a and 6b). However, the total cluster number N decreases as the brine flooding time under the faster flow rate conditions of $Ca = 1.8 \times 10^{-4}$, 3.6×10^{-4}, and 7.5×10^{-4}. For the highest flow rate under the water-wet conditions, the cluster number was very small to begin with because most of the $scCO_2$ had been flushed out. At 80 s of brine flooding, statistically significant differences of N, r_{max}, r_σ, and r_{avg} between water-wet and intermediate-wet micromodels were examined using a two-tailed Student's t test with unequal variance ($^*p \le 0.05$, $^{**}p \le 0.01$), as shown in Figures 6c, 6f, 6i, and 6l. The cluster numbers N in water-wet case are significantly smaller than that in intermediate-wet case under the four flow rate (or Ca) conditions. For the maximum cluster radii r_{max} and the standard deviation of the cluster radii r_σ, significant differences between water-wet and intermediate-wet cases were observed at the lowest flow rate condition (Ca). As Ca increases, however, Figures 6f and 6i show no significant differences of r_{max} as $Ca \ge 1.8 \times 10^{-4}$, and no significant differences of r_σ as $Ca \ge 3.6 \times 10^{-4}$, indicating that the wettability effects on r_{max} and r_σ are suppressed as Ca increases. For the average cluster radius r_{avg} (Figure 6l), there were no significant differences under both the lowest and highest flow rates conditions, while r_{avg} in water-wet case is significantly smaller than that in the intermediate-wet case at $Ca = 1.8 \times 10^{-4}$ and is significantly higher than that in the intermediate-wet case at $Ca = 3.6 \times 10^{-4}$. This demonstrates that the wettability effects on N, r_{max}, and r_σ are not the same as on $r_{avg.}$ The statistical analysis shows that the trapped $scCO_2$ phase in water-wet case is characterized by significantly smaller cluster number for the four Ca conditions, significantly smaller maximum cluster radius, and significantly smaller standard deviation for the lowest Ca of 9.0×10^{-6}.

The cluster radius distributions and the cumulative probability distributions at the brine flooding time of 80 s are reported in Figure 7. From Figure 7d, it can be concluded that the cumulative probability distribution in the water-wet system exhibits a similar trend as that found in intermediate-wet cases, because no significant differences of r_{max}, r_{σ}, r_{avg} for $Ca = 3.6 \times 10^{-4}$ were observed. For the cluster radius distribution, as shown Figures 7a–7d, to provide statistical testing of differences in capillary trapping (section 3.5), we conducted a two-tailed Student's t test for the number of cluster with $r \geq r_0$, where r_0 is the equivalent radius of the pore body in our pore-network, $r_0 =$ 114 μm (Figure 7e). We found the total number of trapped $scCO_2$ clusters with $r \geq r_0$ in intermediate-wet case is significantly larger than that in the water-wet case within 95% confidence intervals (Figure 7e). Giving the common difficulties in obtaining the reservoir relevant low flow rates in micromodel experiments, close attention needs to be paid on the flow rate effect.

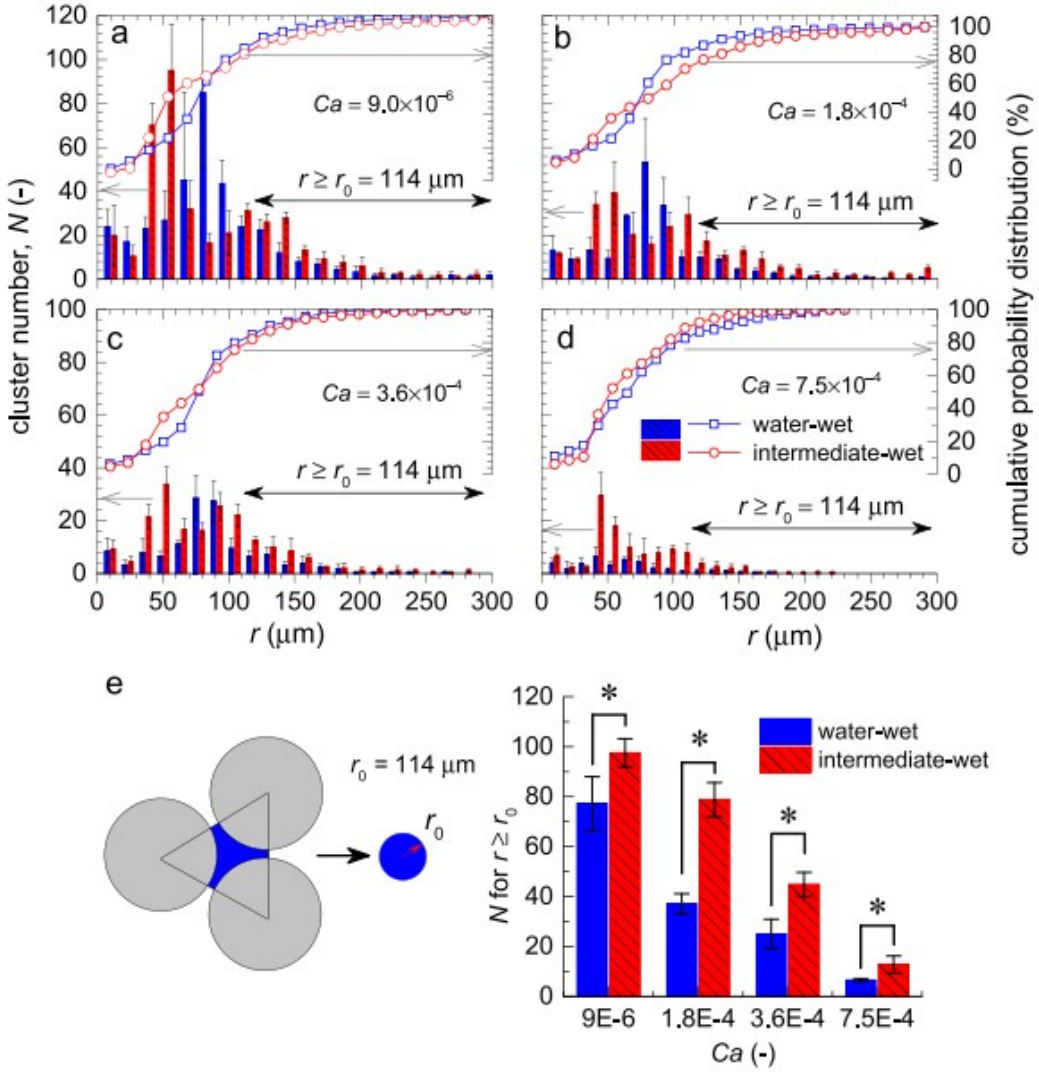

Figure 7. Cluster radius distribution and the cumulative probability distribution in water-wet and intermediate-wet micromodels at 80 s of brine flooding under the capillary numbers of (a) $Ca = 9.0 \times 10^{-6}$, (b) $Ca = 1.8 \times 10^{-4}$, (c) $Ca = 3.6 \times 10^{-4}$, and (d) $Ca = 7.5 \times 10^{-4}$. (e) Two-tailed Student's *t* test with unequal variance for the clusters number *N* with the $r \geq r_0$, where r_0 equivalent radius of a pore body as shown in Figure 7e, $r_0 = 114$ mm; $^*p \leq 0.05$. Each bar indicates the average of four replicate experiments, and the error bars indicate standard deviations. The curves of cumulative cluster radius distribution are calculated from averages of the four replicate experiments.

3.4 The Dependence of $S_{CO_2,f}$ on Capillary Number and Wettability

The $S_{CO_2,f}$ dependence of *Ca* under two different wettability conditions is presented in Figure 8. Figure 8a shows that the trapped $scCO_2$ saturation $S_{CO_2,f}$ in intermediate-wet case is significantly larger than that in the water-wet case for the *Ca* ranging from 9.0×10^{-6} to 7.5×10^{-4}. The average values of $S_{CO_2,f}$ in water-wet case at $Ca = 9.0 \times 10^{-6}$, 1.8×10^{-4}, 3.6×10^{-4}, and 7.5×10^{-4} are, respectively, $27.4 \pm 0.4\%$, $14.4 \pm 0.4\%$, $8.6 \pm 1.1\%$, and $2.7 \pm 0.2\%$, whereas in the intermediate-wet case the values are, respectively, $39.4 \pm 3.3\%$, $25.7 \pm 2.3\%$, $15.0 \pm 0.6\%$, and $5.6 \pm 0.6\%$. The increased $S_{CO_2,f}$ values

decrease from 11.9 to 3.0% as *Ca* increases from 9.0×10^{-6} to 7.5×10^{-4}. As shown in Figure 8b, the measured relation between $S_{CO_2,r}$ and *Ca* follows:

$$S_{CO_2,r} = -\lambda \log_{10} Ca - \beta_0 \cdot (4)$$

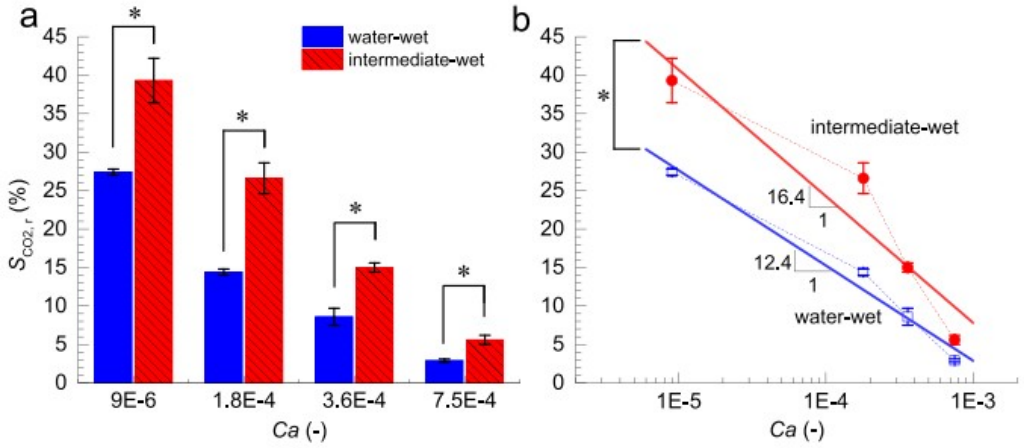

Figure 8. The dependence of $S_{CO_2,r}$ on *Ca* under the water-wet and intermediate-wet conditions. (a) Difference in $S_{CO_2,r}$ between the water-wet and intermediate-wet cases were significant based on a two-tailed Student's *t* test with unequal variance; $*p \leq 0.05$. The bar indicates the average of $S_{CO_2,r}$ of four duplicate experiments, and the error bar indicates the standard deviation. (b) The relation between $S_{CO_2,r}$ and *Ca*. The regression lines are expressed by $S_{CO_2,r} = -12.4\log_{10}(Ca) - 34.2$ ($r^2 = 0.97$) for the water-wet cases, and by $S_{CO_2,r} = -16.4\log_{10}(Ca) - 41.5$ ($r^2 = 0.88$), for the intermediate-wet cases. Statistical comparison of the slopes of two regression lines were conducted based on a Student's *t* test; $*p \leq 0.05$. The dots indicate the average saturations of four replicate experiments, and the error bars indicate standard deviations. All of the $S_{CO_2,r}$ values and the two-tailed Student's *t* test are shown in supporting information Table S1.

In the water-wet case $\lambda = 12.4$, $\beta_0 = 34.2$, while for intermediate-wet case $\lambda = 6.4$, $\beta_0 = 39.5$. Based on Student's *t* test [*Andrade and Estevez-Perez*, 2014], statistical comparison of the slopes (λ) of two regression lines show that the slope of the $S_{CO_2,r}$-$\log_{10}Ca$ curve in the water-wet case is significantly smaller ($p \leq 0.05$) than that in the intermediate-wet case (Figure 8b), indicating that the wettability effect on capillary trapping is effectively suppressed as *Ca* increases.

3.5 Mechanisms Responsible for the Wettability Effect on $scCO_2$ Capillary Trapping

Since the *Ca* in our experiments is higher than the order of 10^{-7} and our micromodels have smooth surfaces [*Kibbey*, 2013; *Geistlinger et al.*, 2016], bypass trapping resulting from engulfment between propagating brine fingers is dominant over pore-scale snap-off trapping caused by the precursor-thin film flow [*Dullien*, 1992; *Geistlinger et al.*, 2015]. In order to test the wettability impact on the bypass trapping mechanism, we selected representative images captured by the DSLR camera for the water-wet and the intermediate-wet cases under the lowest flow rate condition ($Ca = 9.0 \times 10^{-6}$), as shown in Figure 9. These images show brine finger development at the initial stage of brine flooding during which the residual $scCO_2$ phase can be obtained (Figure 5a). Figures 9a and 9b show that the width of brine fingers in intermediate-wet case is ~1*D* ($D = 590$ µm, the diameter of silica grain) with higher velocity of $scCO_2$ front (larger ξ_1, where ξ_1 distance of

brine fingering front from the inlet at $t = 1$ s) whereas the width of brine fingers in water-wet case is ~3D with slower front velocity. Enlarged images of the selected regions (a′ and b′) can help us to better understand the wettability impact on the bypass trapping mechanism. From Figures 9a′ and 9b′, we can clearly observe the immobile $scCO_2$ islands resulting from the bypassing of the brine flow channels. Figures 9a′ and 9b′ also show that the prefilled brine phase surrounded by $scCO_2$ is not affected by the brine invasion. Brine fingers (or channels) with smaller width propagate and bypass relative larger islands of $scCO_2$ phase. This is quantified by our statistical analysis in section 3.4: the maximum size of trapped $scCO_2$ clusters in intermediate-wet case is significantly larger than that in the water-wet case (Figure 6f), and significantly larger numbers of trapped $scCO_2$ clusters whose sizes fall in the range of $r > r_0$ were observed in intermediate-wet case (Figure 7e).

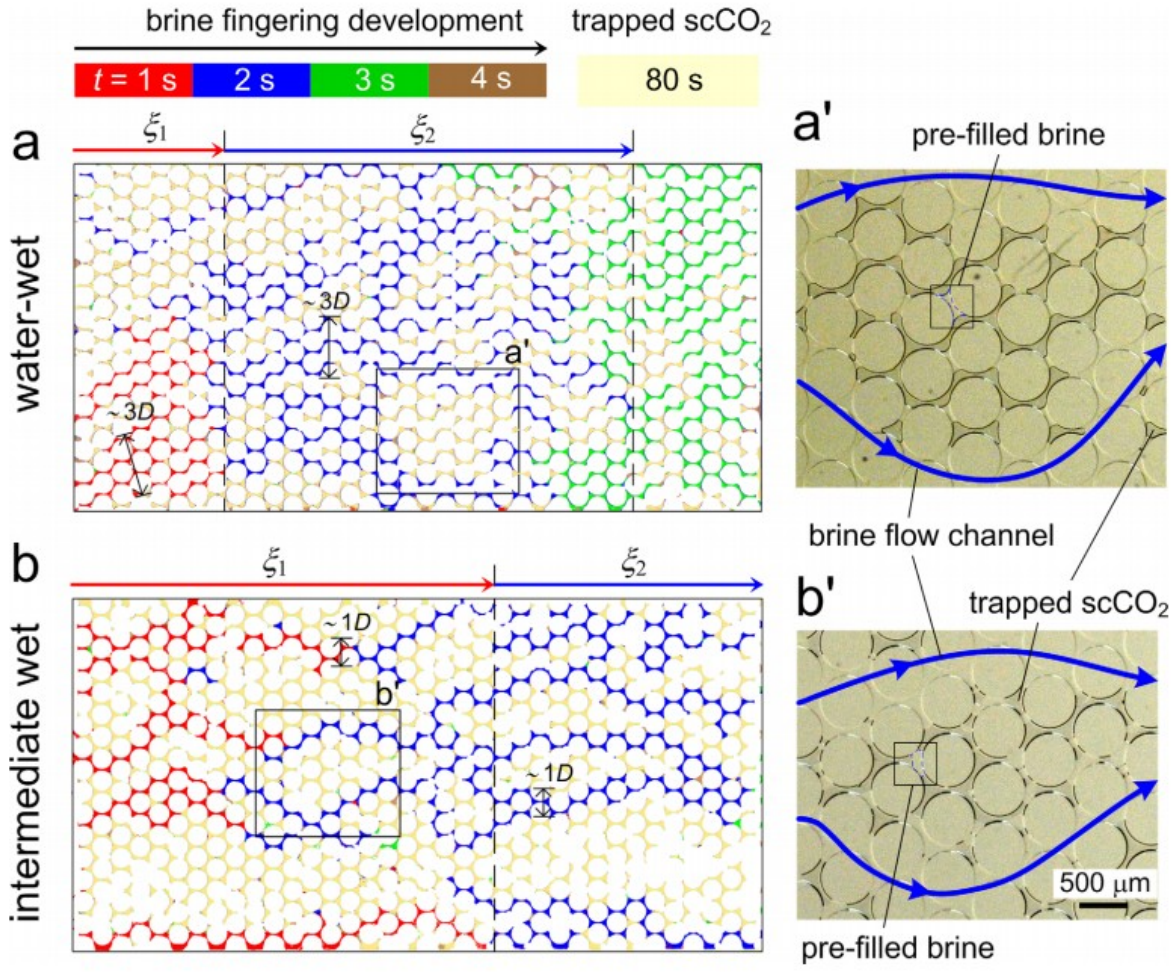

Figure 9. The brine finger development in the (a, a′) water-wet and (b, b′) intermediate-wet micromodels. Relative to the water-wet system. The brine fingers in water-wet case are characterized by smaller width and higher displacement front velocity, which leads to relatively higher $scCO_2$ volume being bypassed. The evolutions of brine invasion morphology at the initial stage of brine flooding are represented by different colors. ξ_1 and ξ_2 are the distances of brine fingering front from the inlet at $t = 1$ s and 2 s, respectively. Note that in Figure 9b, due to the breakthrough of brine fingering, $\xi_1 + \xi_2 = L$, where L is the length of the micromodel.

The observed wider flow channel in water-wet case (Figure 9a) indicates the smaller contact angle of invading fluid will enhance the cooperative pore filling and then suppress the bypass trapping, with less $scCO_2$ phase being trapped. Experimental work suggested that decreasing contact angle of the invading fluid from 90 to 60° will enhance the cooperative events and result in less trapping. The pioneering work by *Cieplak and Robbins* [1988, 1990] under quasi-static simulation recently inspired *Jung et al*. [2016] and *Singh et al*. [2017] to conduct comprehensive experiments with *Ca* ranging from 10^{-4} to 10^{-9} under different wettability conditions. Their results suggest that at the pore scale the smaller contact angle of invading water will favor coalescence of two neighboring menisci into a new meniscus that enlarges the front width at the pore-network scale. This nonlocal (pore-network scale) effect controlled by the local motion of menisci can be well described by the novel pore-scale model of *Holtzman and Segre* [2015]. This nonlocal effect is not captured by the classic pore doublet model [*Chatzis et al*., 1983]. It is worth mentioning that the defending fluid is completely saturated at the start of flooding [*Holtzman and Segre*, 2015; *Jung et al*., 2016], different from our experiment condition where the $scCO_2$ flooding was performed before brine flooding. However, these may only result in small differences because of the high flow rate (1000 μL/min) we applied during $scCO_2$ flooding that would minimize the influence of initial conditions.

Our experiment also shows that the wettability effect on capillary trapping is suppressed as the flow rate increases (Figure 8). This is because the viscous force becomes more influential at high *Ca* and the two-phase immiscible displacement pattern shifts from capillary fingering to viscous-dominated stable displacement [*Lenormand*, 1990] regardless of the water-wet and intermediate-wet conditions. Therefore, the difference of the capillary trapping between the two wettability conditions decreases as *Ca* increases. Moreover, increased flow rates generally facilitate mobilization of trapped phase [*Datta et al*., 2014], and thus the $scCO_2$ cluster numbers and the saturation gradually decrease during brine flooding (Figures 5, 6a, and 6b).

As noted in section 1, although wettability effects on $scCO_2$ capillarity have been intensively studied, evidence for decreased wettability (increased contact angle) resulting in both increased and decreased $scCO_2$ capillary trapping exists in the literature. One group of studies shows that oil-wet or CO_2-wet media trap less $scCO_2$ than the water-wet media [*Iglauer et al*., 2012; *Chaudhary et al*., 2013; *Herring et al*., 2016a; *Rahman et al*., 2016]. However, a second group of studies [*Plug and Bruining*, 2007; *Tokunaga et al*., 2013; *Wang and Tokunaga*, 2015; *Wang et al*., 2016] finds that more nonwetting phase is trapped when porous media become less wetting. For the first group of studies, corner flow with smaller contact angles of the invading fluid may be the dominant mechanism for larger $scCO_2$ volumes being engulfed and trapped, as observed in the $scCO_2$-brine core-flooding experiments [*Chaudhary et al*., 2013] and supported by the water-oil microfluidics experiments [*Zhao et al*., 2016]. Under the strong

imbibition conditions (smaller contact angle), the invading fluid advances along the solid surface [*Zhao et al*., 2016] or through the smaller pores [*Chaudhary et al*., 2013], leading to a larger volume of defending fluid ($scCO_2$ or oil) being trapped.

On the other hand, for the second group, the dominated process under strongly hydrophilic conditions is hypothesized to be cooperative pore-filling [*Cieplak and Robbins*, 1988, 1990; *Holtzman and Segre*, 2015; *Jung et al*., 2016; *Singh et al*., 2017]. In the second group's studies, smaller contact angles enhance cooperative pore-filling, resulting in wider brine fingers that diminish bypass of the defending fluid, and therefore leads to less $scCO_2$ trapped. The overall amounts of trapping reflect these two competing mechanisms operating during imbibition: corner flow with $scCO_2$ engulfment versus cooperative pore filling with $scCO_2$ displacement, with our system described primarily by the latter.

The pore-scale multiphase flow behavior under the imbibition conditions involves additional complications [*Odier et al*., 2017], including influences of pore surface roughness [*Lenormand and Zarcone*, 1984], contact angle hysteresis [*Yu and Wardlaw*, 1986; *Al-Futaisi and Patzek*, 2003], disorder of the porous medium [*Holtzman*, 2016], the initial state CO_2 topology [*Jiang and Tsuji*, 2016], and possible altered wettability during cycles of drainage and imbibition [*Herring et al*., 2016b].

4 Conclusions

We visualized and quantified the wettability impact on the capillary trapping of $scCO_2$ using a high-pressure micromodel-microscopy system. Images of the brine invasion morphology and trapped $scCO_2$ from experiments on water-wet and intermediate-wet homogeneous micromodels prefilled with $scCO_2$ showed the significant effect of wettability on $scCO_2$ capillary trapping. Less water-wet pore surfaces can trap more $scCO_2$, by an additional ~15% of saturation. Our experimental results indicate that bypass trapping is the dominant trapping mechanism in both our water-wet and intermediate-wet micromodels, and that bypass trapping is suppressed by smaller contact angles that enhance the cooperative pore filling leading to wider flow fingers (channels). The wider flow fingers (channels) bypass smaller islands of $scCO_2$ phase and thus less $scCO_2$ volume is trapped. Our experimental results also show that the wettability impact on $scCO_2$ capillary trapping is suppressed as the flow rate increases. We therefore hypothesize that this wettability effect will be amplified by further reducing the brine flooding flow rates to more closely represent typical reservoir conditions ($Ca < 10^{-7}$). This work improves understanding on how wettability affects capillary trapping of $scCO_2$, and is important for GCS because the wettability of rock surfaces can vary from water-wet to intermediate-wet due to sorption of natural organic matter and hydrocarbons, or due to the long-term exposure to $scCO_2$ under reservoir conditions [*Chiquet et al*., 2005; *Plug and Bruining*, 2007; *El-Maghraby and Blunt*, 2012; *Kim et al*., 2012; *Akbarabadi and Piri*, 2013; *Berg*

et al., 2013; *Tokunaga et al*., 2013; *Iglauer et al*., 2015; *Wang and Tokunaga*, 2015]. Other important factors needing investigation include effects of pore and pore-network heterogeneity, mixed wetting, pore-scale immiscible fluid behavior at low *Ca*, and much longer time behavior of trapped CO_2.

Acknowledgments

The study was conducted in the Lawrence Berkeley Laboratory, funded by the Center for Nanoscale Control of Geologic CO_2 (NCGC), an Energy Frontier Research Center (EFRC) of the U.S. Department of Energy, Office of Science, Office of Basic Energy Sciences under award DE-AC02–05CH11231. The first author was also supported by the National Natural Science Foundation of China (grants 51409198 and 51579188). We thank Editor Xavier Sanchez-Vila, Associate Editor Denis O'Carroll, and the anonymous reviewers for their helpful comments and suggestions. Data and images of our experiments supporting this paper can be found in supporting information.

References

Abràmoff, M. D., P. J. Magalhães, and S. J. Ram (2004), Image processing with ImageJ, *Biophotonics Int.*, 11(7), 36– 42.

Akbarabadi, M., and M. Piri (2013), Relative permeability hysteresis and capillary trapping characteristics of supercritical CO_2/brine systems: An experimental study at reservoir conditions, *Adv. Water Resour.*, 52, 190– 206.

Al-Futaisi, A., and T. W. Patzek (2003), Impact of wettability alteration on two-phase flow characteristics of sandstones: A quasi-static description, *Water Resour. Res.*, 39(2), 1042, doi:10.1029/2002WR001366.

Al-Menhali, A. S., and S. Krevor (2016), Capillary trapping of CO_2 in oil reservoirs: Observations in a mixed-wet carbonate rock, *Environ. Sci. Technol.*, 50(5), 2727– 2734.

Anderson, W. (1987), Wettability literature survey: Part 4: Effects of wettability on capillary pressure, *J. Petrol. Technol.*, 39(10), 1283– 1300.

Andrew, M., B. Bijeljic, and M. J. Blunt (2013), Pore-scale imaging of geological carbon dioxide storage under in situ conditions, *Geophys. Res. Lett.*, 40, 3915– 3918, doi:10.1002/grl.50771.

AndradeJ., and Estévez-Pérez, M. (2014), Statistical comparison of the slopes of two regression lines: A tutorial, *Anal. Chim. Acta*, 838, 1– 12.

Andrew, M., B. Bijeljic, and M. J. Blunt (2014a), Pore-by-pore capillary pressure measurements using X-ray microtomography at reservoir conditions: Curvature, snap-off, and remobilization of residual CO_2, *Water Resour. Res.*, 50, 8760– 8774, doi:10.1002/2014WR015970.

Andrew, M., B. Bijeljic, and M. J. Blunt (2014b), Pore-scale imaging of trapped supercritical carbon dioxide in sandstones and carbonates, *Int. J. Greenhouse Gas. Control*, 22, 1– 14.

Armstrong, R. T., A. Georgiadis, H. Ott, D. Klemin, and S. Berg (2014), Critical capillary number: Desaturation studied with fast X-ray computed microtomography, *Geophys. Res. Lett.*, 41, 55– 60, doi:10.1002/2013GL058075.

Bachu, S., and D. B. Bennion (2008), Interfacial tension between CO_2, freshwater, and brine in the range of pressure from (2 to 27) MPa, temperature from (20 to 125) °C, and water salinity from (0 to 334 000) mg L^{-1}, *J. Chem. Eng. Data*, 54(3), 765– 775.

Batzle, M., and Z. Wang (1992), Seismic properties of pore fluids, *Geophysics*, 57(11), 1396– 1408.

Bear, J. (1972), *Dynamics of Fluids in Porous Media*, Elsevier, New York.

Berg, S., H. Ott, S. A. Klapp, A. Schwing, R. Neiteler, N. Brussee, A. Makurat, L. Leu, F. Enzmann, and J.-O. Schwarz (2013), Real-time 3D imaging of Haines jumps in porous media flow, *Proc. Natl. Acad. Sci. U. S. A.*, 110(10), 3755– 3759.

Bikkina, P., J. Wan, Y. Kim, T. J. Kneafsey, and T. K. Tokunaga (2016), Influence of wettability and permeability heterogeneity on miscible CO_2 flooding efficiency, *Fuel*, 166, 219– 226.

Blunt, M. J., and H. Scher (1995), Pore-level modeling of wetting, *Phys. Rev. E*, 52(6), 6387.

Cao, S. C., S. Dai, and J. Jung (2016), Supercritical CO_2 and brine displacement in geological carbon sequestration: Micromodel and pore network simulation studies, *Int. J. Greenhouse Gas Control*, 44, 104– 114.

Chang, C., Q. Zhou, M. Oostrom, T. J. Kneafsey, and H. Mehta (2016a), Pore-scale supercritical CO_2 dissolution and mass transfer under drainage conditions, *Adv. Water Resour.*, 100, 14– 25.

Chang, C., Q. Zhou, T. J. Kneafsey, M. Oostrom, T. W. Wietsma, and Q. Yu (2016b), Pore-scale supercritical CO_2 dissolution and mass transfer under imbibition conditions, *Adv. Water Resour.*, 92, 142– 158.

Chatzis, I., and F. A. L. Dullien (1983), Dynamic immiscible displacement mechanisms in pore doublets: Theory versus experiment, *J. Colloid Interf. Sci.*, 91(1), 199– 222.

Chatzis, I., N. R. Morrow, and H. T. Lim (1983), Magnitude and detailed structure of residual oil saturation, *SPEJ Soc. Pet. Eng. J.*, 23(2), 311– 326.

Chatzis, I., M. Kuntamukkula, and N. Morrow (1988), Effect of capillary number on the microstructure of residual oil in strongly water-wet sandstones, *SPE Reservoir Eng.*, 3(3), 902– 912.

Chaudhary, K., M. B. Cardenas, W. W. Wolfe, J. A. Maisano, R. A. Ketcham, and P. C. Bennett (2013), Pore-scale trapping of supercritical CO_2 and the role of grain wettability and shape, *Geophys. Res. Lett.*, 40, 3878– 3882, doi:10.1002/grl.50658.

Chiquet, P., D. F. Broseta, and S. Thibeau (2005), Capillary alteration of shaly caprocks by carbon dioxide, paper presented at SPE Europec/518 EAGE Annual Conference, *Soc. of Pet. Eng.*, Madrid, Spain.

Cieplak, M., and M. O. Robbins (1988), Dynamical transition in quasistatic fluid invasion in porous media, *Phys. Rev. Lett.*, 60(20), 2042– 2045.

Cieplak, M., and M. O. Robbins (1990), Influence of contact angle on quasistatic fluid invasion of porous media, *Phys. Rev. B*, 41(16), 11508.

Cottin, C., H. Bodiguel, and A. Colin (2011), Influence of wetting conditions on drainage in porous media: A microfluidic study, *Phys. Rev. E*, 84(2), 026311.

Datta, S. S., J.-B. Dupin, and D. A. Weitz (2014), Fluid breakup during simultaneous two-phase flow through a three-dimensional porous medium, *Phys. Fluids*, 26(6), 062004.

Dawson, H. E., and P. V. Roberts (1997), Influence of viscous, gravitational, and capillary forces on DNAPL saturation, *Ground Water*, 35(2), 261– 269.

Dong, M., and I. Chatzis (1995), The imbibition and flow of a wetting liquid along the corners of a square capillary tube, *J. Colloid Interf. Sci.*, 172(2), 278– 288.

Dullien, F. A. (1992), *Porous Media: Fluid Transport and Pore Structure*, Academic Press, New York.

El-Maghraby, R. M., and M. J. Blunt (2012), Residual CO_2 trapping in Indiana limestone, *Environ. Sci. Technol.*, 47(1), 227– 233.

Geistlinger, H., S. Mohammadian, S. Schlueter, and H. J. Vogel (2014), Quantification of capillary trapping of gas clusters using X-ray microtomography, *Water Resour. Res.*, 50, 4514– 4529, doi:10.1002/2013WR014657.

Geistlinger, H., I. Ataei-Dadavi, S. Mohammadian, and H. J. Vogel (2015), The impact of pore structure and surface roughness on capillary trapping for 2-D and 3-D porous media, *Water Resour. Res.*, 51, 9094– 9111, doi:10.1002/2015WR017852.

Geistlinger, H., I. Ataei-Dadavi, and H.-J. Vogel (2016), Impact of surface roughness on capillary trapping using 2d-micromodel visualization experiments, *Transp. Porous Media*, 112(1), 207– 227.

He, S., G. L. Kahanda, and P.-Z. Wong (1992), Roughness of wetting fluid invasion fronts in porous media, *Phys. Rev. Lett.*, 69(26), 3731.

Herring, A. L., A. Sheppard, L. Andersson, and D. Wildenschild (2016a), Impact of wettability alteration on 3D nonwetting phase trapping and transport, *Int. J. Greenhouse Gas Control*, 46, 175– 186.

Herring, A. L., L. Andersson, and D. Wildenschild (2016b), Enhancing residual trapping of supercritical CO_2 via cyclic injections, *Geophys. Res. Lett.*, 43, 9677– 9685.

Holtzman, R. (2016), Effects of pore-scale disorder on fluid displacement in partially-wettable porous media, *Sci. Rep.*, 6, 36221.

Holtzman, R., and E. Segre (2015), Wettability stabilizes fluid invasion into porous media via nonlocal, cooperative pore filling, *Phys. Rev. Lett.*, 115(16), 164501.

Hu, R., J. Wan, Y. Kim, and T. K. Tokunaga (2017), Wettability effects on supercritical CO_2-brine immiscible displacement during drainage: Pore-scale observation and 3D simulation, *Int. J. Greenhouse Gas Control*, 60, 129– 139.

Iglauer, S., M. Fernø, P. Shearing, and M. Blunt (2012), Comparison of residual oil cluster size distribution, morphology and saturation in oil-wet and water-wet sandstone, *J. Colloid Interf. Sci.*, 375(1), 187– 192.

Iglauer, S., C. Pentland, and A. Busch (2015), CO_2 wettability of seal and reservoir rocks and the implications for carbon geo-sequestration, *Water Resour. Res.* 51, 729– 774, doi:10.1002/2014WR015553.

Jamaloei, B. Y., K. Asghari, and R. Kharrat (2012), The investigation of suitability of different capillary number definitions for flow behavior characterization of surfactant-based chemical flooding in heavy oil reservoirs, *J. Petrol. Sci. Eng.*, 90, 48– 55.

Jiang, F., and T. Tsuji (2016), Numerical investigations on the effect of initial state CO_2 topology on capillary trapping efficiency, *Int. J. Greenhouse Gas Control*, 49, 179– 191.

Jimenez-Martínez, J., M. L. Porter, J. D. Hyman, J. W. Carey, and H. S. Viswanathan (2016), Mixing in a three-phase system: Enhanced production of oil-wet reservoirs by CO_2 injection, *Geophys. Res. Lett.*, 43, 196– 205, doi:10.1002/2015GL066787.

Jung, M., M. Brinkmann, R. Seemann, T. Hiller, M. Sanchez de La Lama, and S. Herminghaus (2016), Wettability controls slow immiscible displacement through local interfacial instabilities, *Phys. Rev. Fluids*, 1(7), 074202.

Karadimitriou, N. K. (2013), Two-phase flow experimental studies in micro-models, PhD thesis, Dep. of Earth Sci., Utrecht, Utrecht Univ., Netherlands.

Kazemifar, F., G. Blois, D. C. Kyritsis, and K. T. Christensen (2015), A methodology for velocity field measurement in multiphase high-pressure flow of CO_2 and water in micromodels, *Water Resour. Res.*, 51, 3017– 3029, doi:10.1002/2014WR016787.

Kazemifar, F., G. Blois, D. C. Kyritsis, and K. T. Christensen (2016), Quantifying the flow dynamics of supercritical CO_2–water displacement in a 2D porous micromodel using fluorescent microscopy and microscopic PIV, *Adv. Water Resour.*, 95, 352– 368.

Khishvand, M., M. Akbarabadi, and M. Piri (2016), Micro-scale experimental investigation of the effect of flow rate on trapping in sandstone and carbonate rock samples, *Adv. Water Resour.*, 94, 379– 399, doi:10.1016/j.advwatres.2016.05.012.

Kibbey, T. C. (2013), The configuration of water on rough natural surfaces: Implications for understanding air-water interfacial area, film thickness, and imaging resolution, *Water Resour. Res.*, 49, 4765– 4774, doi:10.1002/wrcr.20383.

Kim, Y., J. Wan, T. J. Kneafsey, and T. K. Tokunaga (2012), Dewetting of silica surfaces upon reactions with supercritical CO_2 and brine: Pore-scale studies in micromodels, *Environ. Sci. Technol.*, 46(7), 4228– 4235.

Kimbrel, E. H., A. L. Herring, R. T. Armstrong, I. Lunati, B. K. Bay, and D. Wildenschild (2015), Experimental characterization of nonwetting phase trapping and implications for geologic CO_2 sequestration, *Int. J. Greenhouse Gas Control*, 42, 1– 15.

Krevor, S., R. Pini, B. Li, and S. M. Benson (2011), Capillary heterogeneity trapping of CO_2 in a sandstone rock at reservoir conditions, *Geophys. Res. Lett.*, 38, L15401, doi:10.1029/2011GL048239.

Krevor, S., M. J. Blunt, S. M. Benson, C. H. Pentland, C. Reynolds, A. Al-Menhali, and B. Niu (2015), Capillary trapping for geologic carbon dioxide storage—From pore scale physics to field scale implications, *Int. J. Greenhouse Gas Control*, 40, 221– 237.

Lenormand, R. (1990), Liquids in porous media, *J. Phys. Condens. Matter*, 2(S), SA79– SA88.

Lenormand, R., and C. Zarcone (1984), Role of roughness and edges during imbibition in square capillaries, paper SPE 13264 presented at 59th Annual Technology Conference, *Soc. of Pet. Eng.*, Houston, Tex.

Lenormand, R., E. Touboul, and C. Zarcone (1988), Numerical models and experiments on immiscible displacements in porous media, *J. Fluid Mech.*, 189, 165– 187.

Li, X., M. Akbarabadi, Z. Karpyn, M. Piri, and E. Bazilevskaya (2015), Experimental investigation of carbon dioxide trapping due to capillary retention in saline aquifers, *Geofluids*, 15(4), 563– 576.

Metz, B. (2005), *IPCC Special Report on Carbon Dioxide Capture and Storage*, Cambridge Univ. Press, Cambridge, U. K.

Morrow, N. R. (1990), Wettability and its effect on oil recovery, *J. Petrol. Technol.*, 42(12), 1476– 1484.

Ng, K., and A. Payatakes (1980), Stochastic simulation of the motion, breakup and stranding of oil ganglia in water-wet granular porous media during immiscible displacement, *AIChE J.*, 26(3), 419– 429.

Niu, B., A. Al-Menhali, and S. C. Krevor (2015), The impact of reservoir conditions on the residual trapping of carbon dioxide in Berea sandstone, *Water Resour. Res.*, 51, 2009– 2029, doi:10.1002/2014WR016441.

Odier, C., B. Levaché, E. Santanach-Carreras, and D. Bartolo (2017), Forced imbibition in porous media: A fourfold scenario, *arXiv:* 1705.07775.

Otsu, N. (1975), A threshold selection method from gray-level histograms, *Automatica*, 11(285–296), 23– 27.

Pachauri, R. K., M. Allen, V. Barros, J. Broome, W. Cramer, R. Christ, J. Church, L. Clarke, Q. Dahe, and P. Dasgupta (2014), Climate change 2014: synthesis report. Contribution of working groups I, II and III to the fifth assessment report, the Intergovernmental Panel on Climate Change, IPCC, Geneva, Switzerland.

Pak, T., I. B. Butler, S. Geiger, M. I. van Dijke, and K. S. Sorbie (2015), Droplet fragmentation: 3D imaging of a previously unidentified pore-scale process during multiphase flow in porous media, *Proc. Natl. Acad. Sci. U. S. A.*, 112(7), 1947– 1952.

Patzek, T. W., F. Male, and M. Marder (2013), Gas production in the Barnett Shale obeys a simple scaling theory, *Proc. Natl. Acad. Sci. U. S. A.*, 110(49), 19,731– 19,736.

Pentland, C. H., R. El-Maghraby, S. Iglauer, and M. J. Blunt (2011), Measurements of the capillary trapping of super-critical carbon dioxide in Berea sandstone, *Geophys. Res. Lett.*, 38, L06401, doi:10.1029/2011GL046683.

Philip, J. (1971), Limitations on scaling by contact angle, *Soil Sci. Soc. Am. J.*, 35(3), 507– 509.

Plug, W.-J., and J. Bruining (2007), Capillary pressure for the sand–CO_2–water system under various pressure conditions. Application to CO_2 sequestration, *Adv. Water Resour.*, 30(11), 2339– 2353.

Rahman, T., M. Lebedev, A. Barifcani, and S. Iglauer (2016), Residual trapping of supercritical CO_2 in oil-wet sandstone, *J. Colloid Interf. Sci.*, 469, 63– 68.

Saadatpoor, E., S. L. Bryant, and K. Sepehrnoori (2010), New trapping mechanism in carbon sequestration, *Transp. Porous Media*, 82(1), 3– 17.

Simjoo, M., Y. Dong, A. Andrianov, M. Talanana, and P. Zitha (2013), CT scan study of immiscible foam flow in porous media for enhancing oil recovery, *Ind. Eng. Chem. Res.*, 52(18), 6221– 6233.

Singh, K., H. Scholl, M. Brinkmann, M. D. Michiel, M. Scheel, S. Herminghaus, and R. Seemann (2017), The role of local instabilities in fluid invasion into permeable media, *Sci. Rep.*, 7(1), 444.

Soroush, M., D. Wessel-Berg, O. Torsaeter, and J. Kleppe (2014), Investigating residual trapping in CO_2 storage in saline aquifers—Application of a 2D glass model, and image analysis, *Energy Sci. Eng.*, 2(3), 149– 163.

Spiteri, E. J., R. Juanes, M. J. Blunt, and F. M. Orr (2008), A new model of trapping and relative permeability hysteresis for all wettability characteristics, *SPE J.*, 13(3), 277– 288.

Tanino, Y., and M. J. Blunt (2012), Capillary trapping in sandstones and carbonates: Dependence on pore structure, *Water Resour. Res.*, 48, W08525, doi:10.1029/2011WR011712.

Teng, Y., Y. Liu, L. Jiang, G. Lu, D. Wang, and Y. Song (2016), CO_2 capillary trapping behaviour in glass sand packed heterogeneous porous media during drainage and imbibition revealed by magnetic resonance imaging, *RSC Adv.*, 6, 101452.

Tokunaga, T. K., and J. Wan (2013), Capillary pressure and mineral wettability influences on reservoir CO_2 capacity, *Rev. Mineral. Geochem.*, 77(1), 481– 503.

Tokunaga, T. K., J. Wan, J. W. Jung, T. W. Kim, Y. Kim, and W. Dong (2013), Capillary pressure and saturation relations for supercritical CO_2 and brine in sand: High-pressure Pc (Sw) controller/meter measurements and capillary scaling predictions, *Water Resour. Res.*, 49, 4566– 4579, doi:10.1002/wrcr.20316.

Trojer, M., M. L. Szulczewski, and R. Juanes (2015), Stabilizing fluid-fluid displacements in porous media through wettability alteration, *Phys. Rev. Appl.*, 3(5), 054008.

Wang, S., and T. K. Tokunaga (2015), Capillary pressure-saturation relations for supercritical CO_2 and brine in limestone/dolomite sands: Implications for geologic carbon sequestration in carbonate reservoirs, *Environ. Sci. Technol.*, 49(12), 7208– 7217.

Wang, S., T. K. Tokunaga, J. Wan, W. Dong, and Y. Kim (2016), Capillary pressure-saturation relations in quartz and carbonate sands: Limitations for correlating capillary and wettability influences on air, oil, and supercritical CO_2 trapping, *Water Resour. Res.*, 52, 6671– 6690, doi:10.1002/2016WR018816.

Wang, Y., C. Zhang, N. Wei, M. Oostrom, T. W. Wietsma, X. Li, and A. Bonneville (2012), Experimental study of crossover from capillary to viscous fingering for supercritical CO_2–water displacement in a homogeneous pore network, *Environ. Sci. Technol.*, 47(1), 212– 218.

Wardlaw, N., and M. McKellar (1985), Oil blob populations and mobilization of trapped oil in unconsolidated packs, *Can. J. Chem. Eng.*, 63(4), 525– 532.

Weislogel, M. M., and S. Lichter (1998), Capillary flow in an interior corner, *J. Fluid Mech.*, 373, 349– 378.

Wong, P.-Z. (1994), Flow in porous media: Permeability and displacement patterns, *MRS Bull.*, 19(05), 32– 38.

Xu, T., J. A. Apps, and K. Pruess (2005), Mineral sequestration of carbon dioxide in a sandstone–shale system, *Chem. Geol.*, 217(3), 295– 318.

Xu, W., J. T. Ok, F. Xiao, K. B. Neeves, and X. Yin (2014), Effect of pore geometry and interfacial tension on water-oil displacement efficiency in oil-wet microfluidic porous media analogs, *Phys. Fluids*, 26(9), 093102.

Yu, L., and N. C. Wardlaw (1986), The influence of wettability and critical pore-throat size ratio on snap-off, *J. Colloid Interf. Sci.*, 109(2), 461– 472.

Zhang, C., M. Oostrom, J. W. Grate, T. W. Wietsma, and M. G. Warner (2011a), Liquid CO_2 displacement of water in a dual-permeability pore network micromodel, *Environ. Sci. Technol.*, 45(17), 7581– 7588.

Zhang, C., M. Oostrom, T. W. Wietsma, J. W. Grate, and M. G. Warner (2011b), Influence of viscous and capillary forces on immiscible fluid displacement: Pore-scale experimental study in a water-wet micromodel demonstrating viscous and capillary fingering, *Energy Fuel*, 25(8), 3493– 3505.

Zhao, B., C. W. MacMinn, and R. Juanes (2016), Wettability control on multiphase flow in patterned microfluidics, *Proc. Natl. Acad. Sci. U. S. A.*, 113(37), 10,251– 10,256.

Zuo, L., and S. M. Benson (2014), Process-dependent residual trapping of CO_2 in sandstone, *Geophys. Res. Lett.*, 41, 2820– 2826, doi:10.1002/2014GL059653.